Advances and Challenges in Single-Site Catalysts towards Electrochemical CO_2 Methanation

Jiexin Zhu[a,b], Lei Lv[a], Shahid Zaman[e], Xingbao Chen[a], Yuhang Dai[a,b], Shenghua Chen,[c] Guanjie He[b], Dingsheng Wang,[d]* Liqiang Mai[a]**

[a]State Key Laboratory of Advanced Technology for Materials Synthesis and Processing, Wuhan University of Technology, Wuhan 430070, China

[b]Electrochemical Innovation Lab, Department of Chemical Engineering, University College London, London, WC1E 7JE, UK

[c]National Innovation Platform (Center) for Industry-Education Integration of Energy Storage Technology, Xi'an Jiaotong University, Xi'an, P. R. 710049, China.

[d]Department of Chemistry, Tsinghua University, Beijing 100084, China.

[e]Department of Mechanical and Energy Engineering, Southern University of Science and Technology, Shenzhen 518055, China.

[e]

Email: shenghchen@163.com; wangdingsheng@mail.tsinghua.edu.cn; mlq518@whut.edu.cn

Abstract

The electrochemical CO_2 reduction into a valuable product is a sustainable and economical method towards carbon neutralization. Among the different products of electrochemical CO_2 reduction reaction (CO_2RR), methane is an excellent energy carrier with a high combustion heat. However, for higher methane product selectivity it is crucial to avoid C–C coupling that leads to multi-carbon products. Thus, single-site catalysts (SSCs) with a single active site are ideal candidates. This review summarizes and discusses the current research progress and future applications prospect of electrochemical CO_2 methanation on SSCs. CO_2 methanation mechanism and primary activity descriptors are discussed in detail with an extensive overview of SSCs coordination structure and design, as well as several in-situ characterizations for tracking the structural change in SSCs. This review provides insights into the further exploitation of SSCs for selective CO_2 methanation that inspires the rational design of SSCs in electrochemical CO_2 methanation research.

Keywords: Single-site catalysts, CO_2 electroreduction, methane production, coordination structure design, in-situ characterizations

Broder context

Electrochemical CO_2 reduction reaction powered by renewable energy offers a promising pathway to produce valuable chemical feedstocks which may control and utilize atmospheric CO_2 emissions. Among the CO_2RR products, CH_4 is a good energy carrier with the highest combustion heat of 56 KJ/g. To achieve high selectivity for CH_4, the *CO-CO coupling on multisites should be avoided. Single site catalysts are idea candidates for CO_2 methanation due to their sites isolation properties. However, the deep reduuction of CO_2 on single site is difficult and reaction mechanism is complex. Unrevealing the activity descriptors for CO_2 methanation can help us understanding the reaction mechanism and proposing appropriate design strategies for single site catalysts. In this review, we discuss the activity descriptors based on the reaction mechanism and the design strategies of single site catalysts. The development of in-situ characterizations are also discussed to monitor the structural change of single site catalysts. This review provides a guideline for the design, charactieriztaion, and application of single site catalysts.

1. Introduction

The widespread consumption of fossil fuels poses an enormous risk to the global environment. Chemical industries manufacture chemical products using fossil fuel-derived feedstocks, accounting for 18% of today's industrial CO_2 emissions, with coal combustion being the primary source of CO_2.[1-4] A series of climatic changes have been triggered by the progressive increase in atmospheric CO_2 emissions, causing an increase in global temperatures. Meanwhile, it is indispensable to halt the average increased in global temperatures below 1.5 °C by reducing atmospheric CO_2 emissions.[5] Therefore, converting atmospheric CO_2 into valuable chemical feedstocks is a sustainabble approach for controlling and utilizing atmospheric CO_2 emissions.[6] Moreover, electricity costs will drop significantly with the development of solar and wind energy conversion and storage. Therefore electrochemical CO_2 reduction reaction (CO_2RR) driven by renewable energy presents a feasible route to manufacture valuable chemical feedstocks (**Figure 1**).[7-17] A typical CO_2RR process comprises CO_2 conversion into a series of short carbon chain molecules such as carbon monoxide (CO), formic acid (HCOOH), methane (CH_4), ethylene (C_2H_4), ethanol (C_2H_5OH), propanol (C_3H_7OH) etc.[18-21] These molecule feedstocks can fuel or produce chemical products in traditional chemical enterprises.

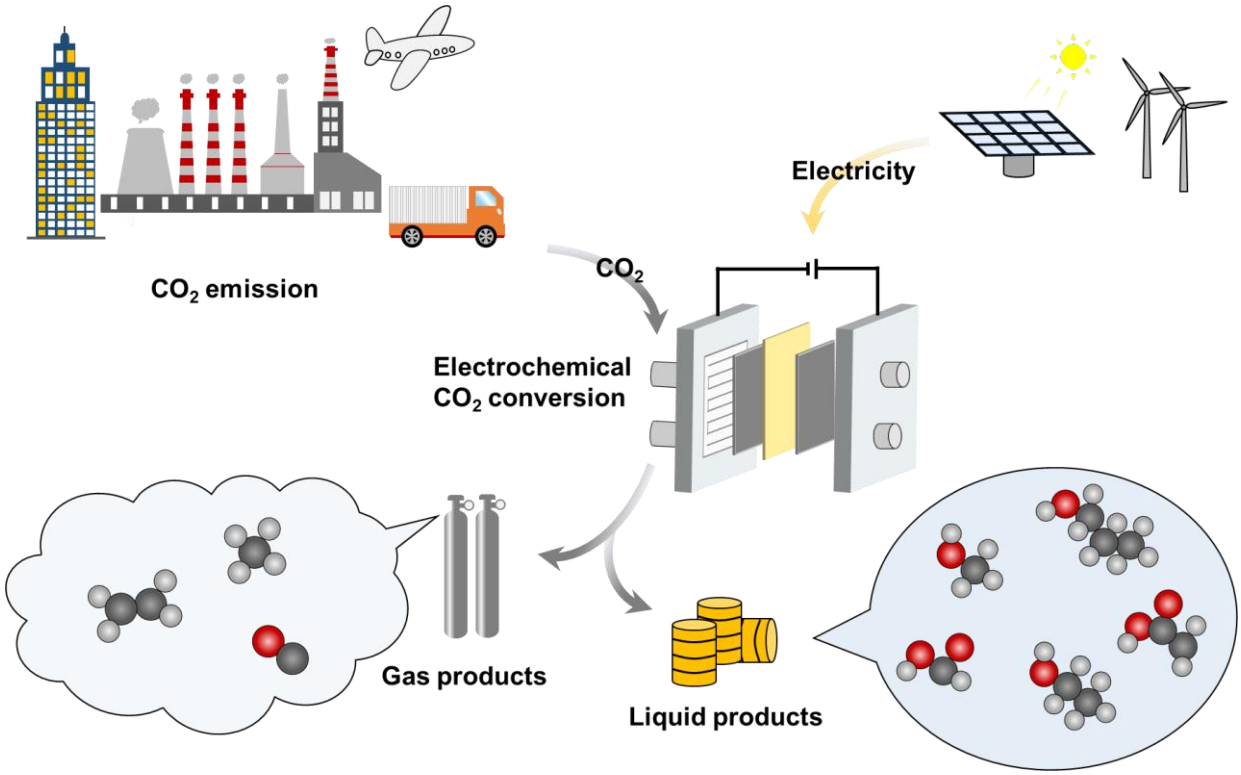

Figure 1. CO_2 utilization pathway using electricity produced from renewable energy.

Among the CO_2RR products, CH_4 is a suitable energy carrier with the highest combustion heat of 56 KJ/g.[22, 23] It is also a main component of natural gas and a clean energy source that reduces the

use of fossil fuels and can be used as feedstocks to produce carbon black, ammonia, urea, etc.[24] Besides, CH_4 is a typical greenhouse effect gas, and the greenhouse effect caused by 1% of methane will be greater than that of 99% of CO_2. Due to the unreasonable mining, a large amount of CH_4 is directly leaked into the atmosphere. Therefore, producing CH_4 from CO_2RR can regulate the CO_2 level in atmosphere and decrease natural gas utilization and leakage, thus reducing the greenhouse effect. Apart from the the electrochemical CO_2 methanation, thermocatalytic reduction of CO_2 into CH_4 with H_2 produced via water electrolysis is also a common way.[25-27] The electrochemical CO_2 reduction always proceed at room temperature, whereas thermocatalytic CO_2 transformation typically necessitates high pressure and elevated temperatures, typically within the range of 200−300 °C. The high operate temperature cost a lot of energy, and the water electrolysis produced H_2 require extra storage and transportation. In contrast, the electrochemical CO_2 methanation which consume cheap electricity and protons from electrolytes represent a more ecomonical and simpler route. For the selective CH_4, electrochemical CO_2RR involves eight-electron transfer with the standard equilibrium potential of 0.17 V vs. reversible hydrogen electrode (RHE), which is a more favorable product. However, due to the sluggish multi-electron transfer and electron-proton coupling efficiency, the practical activity for CO_2 methanation is far from the equilibrium potential.[28] Besides, the competitive relationship between hydrogen evolution reaction (HER) further reduces the CO_2RR selectivity.

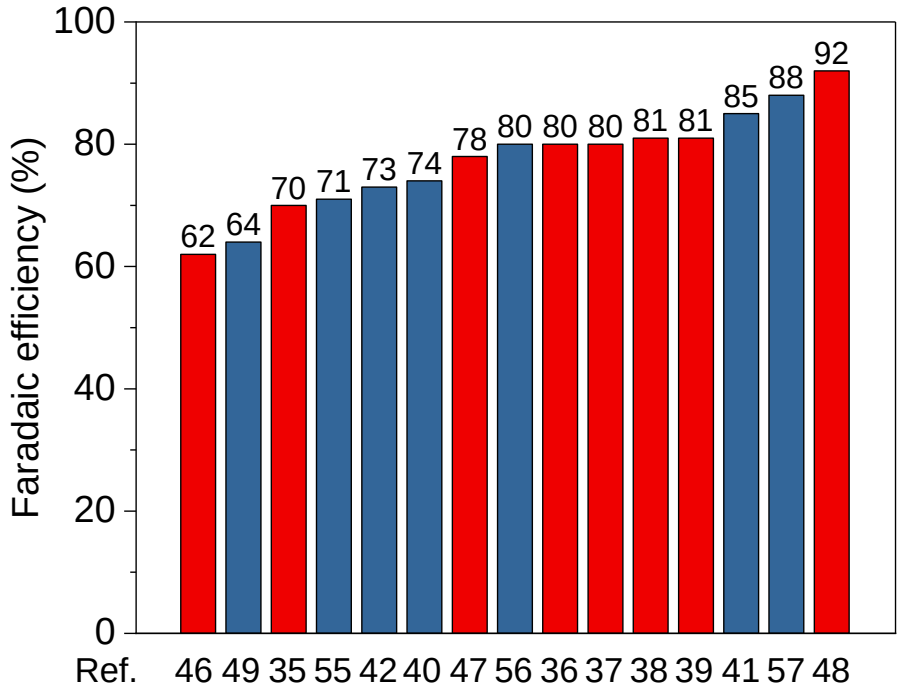

Figure 2. The reported electrocatalysts with high CH_4 selectivity of CO_2RR in recent years. The red columns represent the SSCs, and the blue columns represent the other catalysts.

Therefore, it is vital to identify prospective electrocatalysts with high activity and selectivity to lower the energy barrier of CO_2 methanation.[29-31] Most electrocatalysts lack the ability to stabilize important intermediates such as *CHO and *COOC, which is required for the reduction reaction to progress beyond two-electron transfer, making copper (Cu)-based electrocatalysts superior.[20, 32-45] However, Cu-based electrocatalysts are more vibrant to reduce CO_2 into ethanol and ethylene due to the facile *CO-CO coupling step on the Cu surface. Furthermore, the slow eight-electron transfer and the competitive HER both inhibit CO_2 methanation. As a result, it is challenging to attain high faradaic efficiency (FE) exceeding 90% on Cu electrocatalysts, which is much lower on other electrocatalysts.

Despite these problems, the FE for CO_2 methanation has significantly increased over the past decade, showing that 80% or higher FE is relatively simple to accomplish. It is found that a higher CO_2 methanation selectivity can be achieved on SSCs (**Figure 2**).[35-39, 46-57] We take for granted that isolated sites cannot achieve the *CO-CO coupling step so that the further reduction of *CO can proceed. The multi-electron transfer step can be pushed gradually through appropriate electronic structure optimizations. However, limited active sites, complex coordination structure, weak electron transfer capacity, and structural instability of SSC restrict the CH_4 selectivity of CO_2RR. To achieve higher FE for CH_4, it is vital to identify the critical CO_2 methanation paremeters and the structure-activity relationship of SSCs.

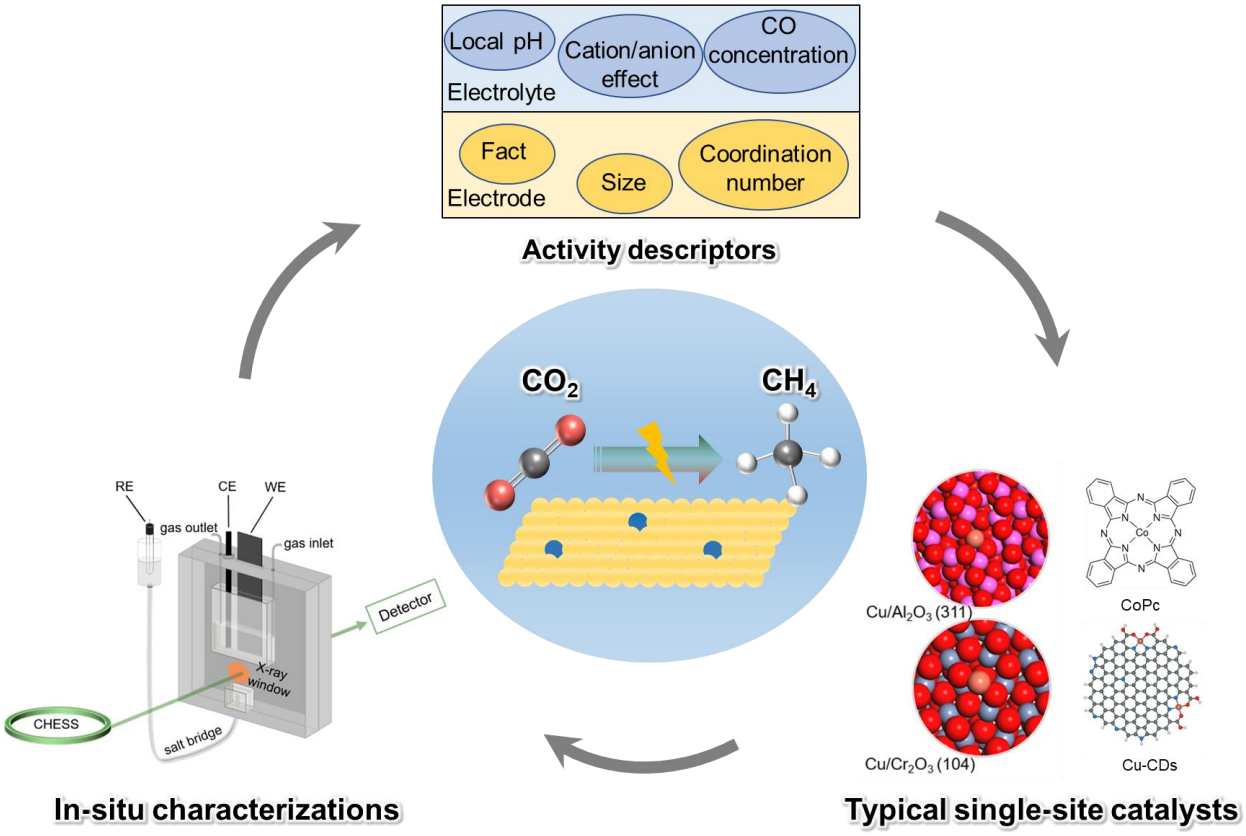

Figure 3. A schematic outline of the key topics covered in this study.

This review systematically summarizes the recent advances and challenges of electrocatalytic CO_2 methanation on SSCs (**Figure 3**). Firstly, we discuss the key parameters which greatly influence the selectivity of CO_2 methanation, including catalysts factor: facet-dependence, size effect, coordination number, and local reaction environment factor: local pH, anions/cations effect, and CO concentration. The recent advances of SSCs on different substrates for electrocatalytic CO_2 methanation, especially the molecule-based and carbon-supported electrocatalysts, highlight the engineering in coordination and electronic structures. Furthermore, various in-situ characterizations for tracking the structure change of SSCs during CO_2RR are introduced, such as in-situ XAS and in-situ Raman spectroscopy. Finally, challenges and outlooks on electrocatalytic CO_2 methanation industrialization are discussed.

2. Key parameters for electrocatalytic CO_2 methanation

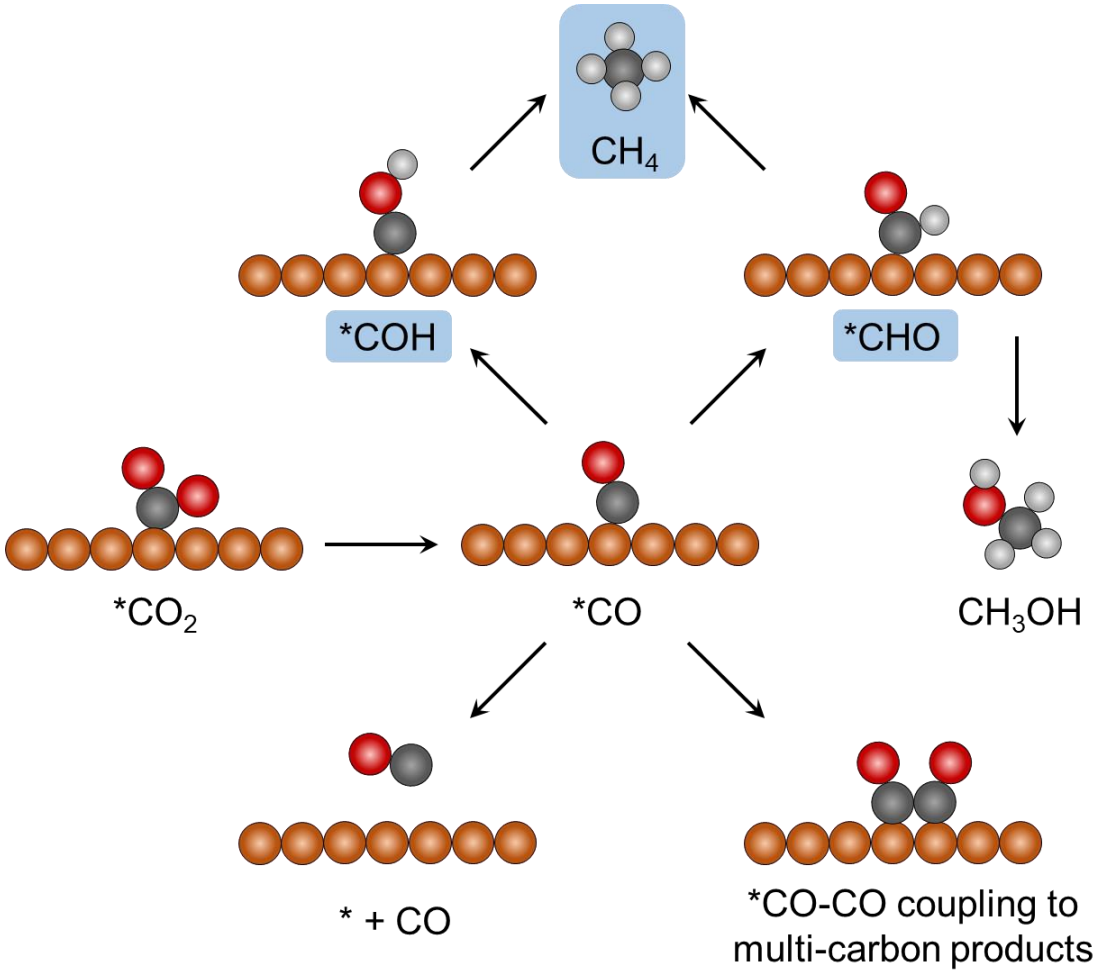

Figure 4. The reaction pathways derived from the *CO intermediate on Cu-based catalysts.

The reduction of CO_2 into valuable products involves multiple electrons and protons transfer, and the product selectivity continuously decreases as the required number of electrons and protons increases. For the CH_4 product, eight electrons and protons are needed, indicating that the CO_2

methanation is a high-energy barrier process. Although the CO_2 methanation possesses the most positive thermodynamic potential than other products, it is also limited by the formation of $*CO_2^-$ intermediate. The first electron transfer to the adsorbed $*CO_2$ shows an equilibrium potential as negative as –1.9 V (vs. the standard hydrogen electrode, SHE). Therefore, the onset potential for CO_2 methanation is always more negative than that of CO, formic acid, and C_2H_4.[58, 59] Thus, the reaction pathway of CO_2 methanation involves *CO intermediate.[18, 60, 61] *CO is a key intermediate for many products that can be desorbed from the catalyst surface to form a CO molecule, or it can form a *CO-CO dimer and then be reduced to multi-carbon products like C_2H_4 and C_2H_5OH (**Figure 4**). Thus, to obtain CH_4 in the subsequent step, the formation of *COH or *CHO is necessary.[62] The *COH pathway can only yield CH_4, while the *CHO pathway can also result in CH_3OH formation. Therefore, the direction of further reduction of *CO intermediate is crucial for product selectivity. Several key parameters profoundly affect the reaction pathways for CO_2 methanation, including the catalysts factor: facet-dependence, size effect, coordination number, and local reaction environment factor: local pH, CO concentration, and anions/cations effect.

2.1 Facet-dependence

Facet-dependence is a common characteristic of many chemical reactions on metal catalysts.[63] Earlier experiments found that CH_4 is formed more favorably on the Cu (100) surface, and C_2H_4 is predominantly produced on the Cu (111) surface.[64, 65] Similarly, the CH_4 formation is advantageous when the electrode is covered with abundant protons or hydrogen species.[58] Density functional theory (DFT) calculation has explored the specific impact of $H_3O^{\delta+}$ species on the products selectivity on Cu (100) and Cu (111) surfaces,[62] finding that the CO_2 is firstly adsorbed and reduced to *CO. However, the hydrogenation of *CO is different in each facet. On Cu (100), the formation of *CHO is favored and the product of ethylene is preferred by going through the C–C coupling of two *CHO intermediates. Cu (111) favors the formation of *COH, and methane is the dominant product. The formation of *CHO and *COH involve an H transferred from the solution to the adsorbed *CO intermediate. The supplied H comes from the metal surface for *CHO formation, while it comes from the water molecule in solution for the *COH formation. The hydrogenation process shows different configurations on Cu (100) and Cu (111) (**Figure 5a, b**). In transition states, two Cu atoms are close to the $H_3O^{\delta+}$ species on both Cu (100) and Cu (111). Due to the hexagonal configuration of the Cu (111) surface, additional two Cu atoms are close to $H_3O^{\delta+}$ species with distances of 2.62 and 2.81 Å (**Figure 5c**). The different configurations result in the bonding of $H_3O^{\delta+}$ on Cu (100) an ionic bond and it is a covalent bond on Cu (111), which leads to a more stable $H_3O^{\delta+}$ on Cu (111) and reduces the barrier of *COH formations.

For SSCs, the facet-dependence is rarely discussed because the metal site in SSC is isolated. However, the coordination configuration of H towards *CO determined by facet can be extended to SCCs. Adjusting the ligand structure or coordinated atoms to the metal site can alter the bonding structure of H species and *CO intermediate and steer the product selectivity.

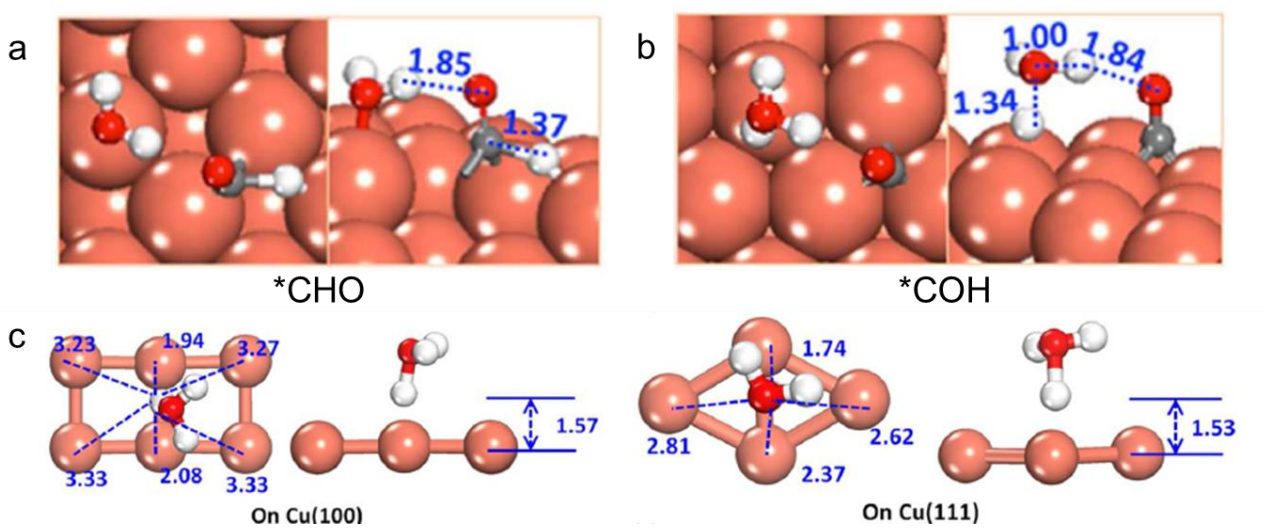

Figure 5. Optimized structures of the transition states involved in *CO reduction to (a) *CHO with the water-solvated model on Cu (100) facet and to (b) *COH with the H-shuttling model on the Cu (111) facet. (c) Closeup of the $H_3O^{\delta+}$ moiety in the transition state of COH* formation on Cu(100) and Cu(111). Reproduced with permission from Asthagiri *et al.*[62] Copyright 2016 American Chemical Society.

2.2 Size effect

Tuning the size and shape of catalysts is a well-known strategy to alter the binding energy of catalysts surface to reactants.[66-75] The size effect has been wildly studied in thermocatalytic reactions, such as ammonia synthesis and hydrogenations.[76-78] However, it is challenging to determine the effect of nanoparticle size on catalytic performance in electrocatalytic processes since the negative or positive potential always leads to structural reconstruction of electrocatalysts. The size effects on CH_4 selectivity for CO_2RR were investigated by comparing the reconstruction and performances of Cu nanoparticles supported on glassy carbon (n-Cu/C) and Cu foil.[79] It is found that the n-Cu/C and Cu foil undergoes a structural transformation during CO_2RR condition, resulting in increased nanoparticles size (from 7.0 nm to 23 ± 8 nm) (**Figure 6a, b**). Interestingly, even a larger particle with a 52 ± 21 nm diameter is reconstructed into 25 ± 8 nm during CO_2RR. Furthermore, the n-Cu/C displays a CH_4 selectivity of 76%, higher than the FE of 44% on Cu foil (**Figure 6c**). Different thicknesses of Cu film prepared on glass carbon uncover the size effect on catalytic performances, where the evaporated Cu films also undergo a severe structural transformation during CO_2RR.

Isolated nanoscale particles appeared on the thin film (**Figure 6d**), while the thick film produced numerous fused nanoparticles (**Figure 6e**) under CO_2RR conditions. In contrast, the thin film shows a FE of CH_4 similar to the n-Cu/C, and the thick film shows a low FE of CH_4 (**Figure 6f**). These studies prove that tiny particles or isolated nanoparticles possess higher activity and selectivity toward CH_4 formation.

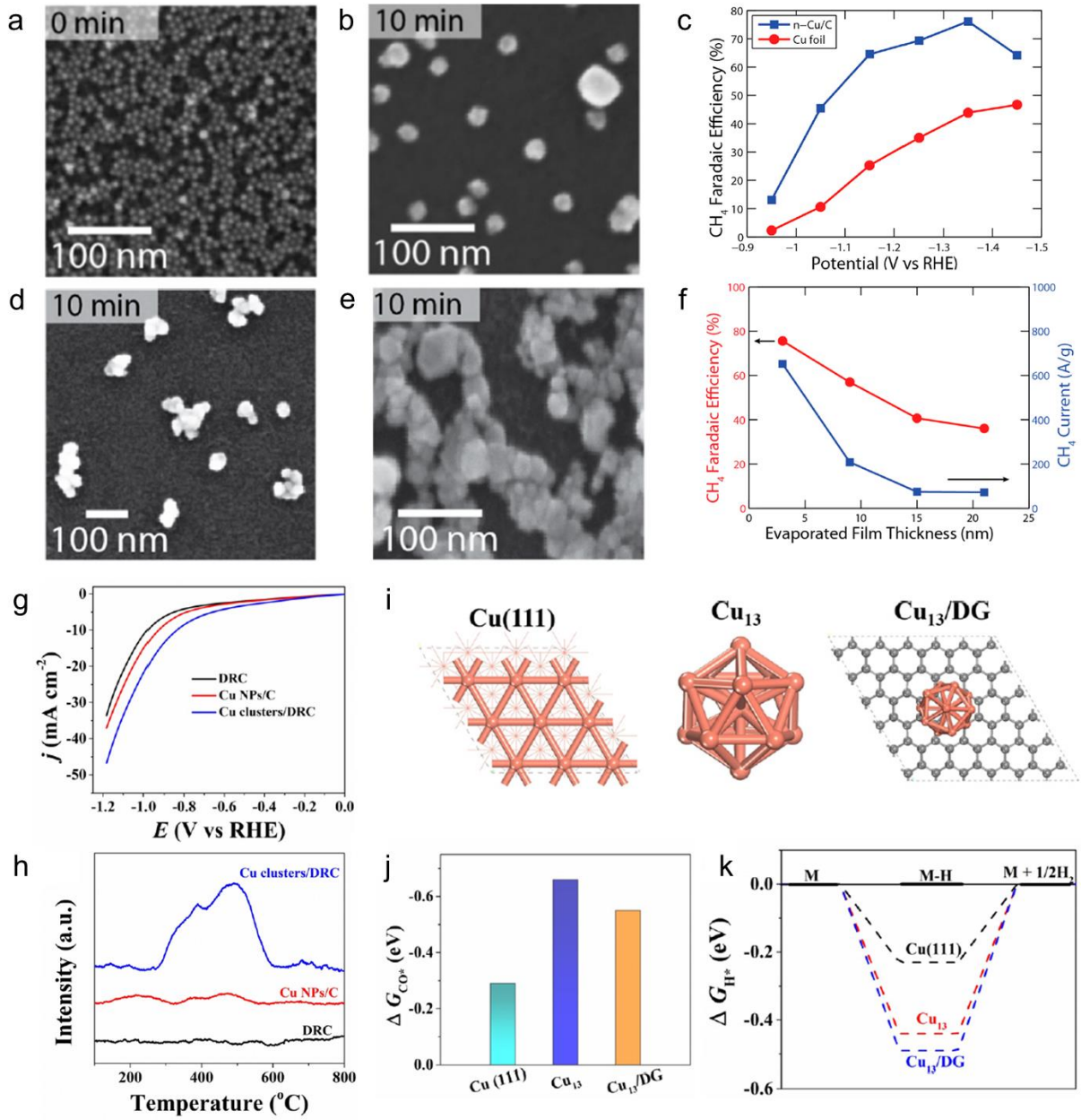

Figure 6. (a) SEM image of the n-Cu/C electrode and (b) following an operation for 10 min at −1.25 V vs. RHE under CO_2RR conditions. (c) FE for CH_4 on n-Cu/C Cu foil. (d) 3 nm evaporated Cu film after operating at −1.25 V for 10 min. (e) 15 nm evaporated Cu film after operating at −1.25 V for 10 min. (f) FE and mass current density for CH_4 as a function of evaporated Cu film thickness. Reproduced with permission from Alivisatos *et al.*[79] Copyright 2014 American Chemical Society. (g) LSV of DRC, Cu NPs/C, and Cu clusters/DRC for the CO_2RR. (h) H_2-TPD curves of DRC, Cu NPs/C,

and Cu clusters/DRC. (i) Optimized structural model of Cu (111), Cu_{13}, and Cu_{13}/DG. Adsorption energies of (j) *CO and (k) *H intermediates on the above three models. Reproduced with permission from Alivisatos *et al.*[80] Copyright 2020 Wiley-VCH GmbH

Reducing the size of electrocatalysts and keeping it dispersed can affect the binding energy of catalysts to reaction intermediates. Sub-nanometric Cu clusters dispersed on the defective-rich carbon (Cu clusters/DRC) show the highest current density (**Figure 6g**) and a maximum FE of 81.7% for CH_4. Reducing the size of catalysts leads to the upshift of the *d*-band center, thus improving the adsorption intensity of some specific intermediates. To enhance the CH_4 selectivity, H species should be fed for the protonation of *CO rather than for H_2 production. As shown in **Figure 6h**, the Cu clusters/DRC offers a board peak at the temperature range of 265 ~ 611 °C in the temperature-programmed desorption of H_2 (H_2-TPD) test, indicating the strong adsorption capacity of H species, which hinders the desorption of *H for H_2 formation. DFT calculations (**Figure 6i**) reveal that the adsorption energies of *CO and *H (ΔG_{CO*} and ΔG_{H*}) on Cu (111) are much higher than those on the C_{13} clusters and Cu_{13}/DG (**Figure 6j, k**). The Cu clusters possess stronger adsorption strength to *CO and *H intermediates, which are the precursors to obtaining the key intermediate of *CHO for CH_4 production. Therefore, it is rational to regard that single metal sites may have better CH_4 selectivity than nanoparticles.

2.3 Coordination number

The catalytic reaction involves the orbital interaction between catalysts and reactants, and thus the coordination number (CN) of catalysts significantly impacts the catalytic performance.[18, 66, 81-88] The comparative investigattion on the relationship between facet, CN, and product selectivity using DFT calculations show that the CH_4 formation is favorable on the Cu (111) plane and some steps in either direction with high CN of 9 (**Figure 7a**).[89] The products of C_2H_4 and C_2H_5OH tend to form on the plane with lower CN compared to that of CH_4 (**Figure 7b, c**). Similiarly, the atomic modeling analysis of the surface atomic CN of spherical Cu nanoparticles demonstrates size-dependent populations of atoms with CN.[67] When the size of nanoparticles reduces to ultrafine, the low coordinated atoms ($CN \leq 9$) become dominant, especially the atoms with $CN < 8$ are drastically augmented below 2 nm (**Figure 7d, e**). The contribution of several CN is relatively even on Cu nanoparticles with a diameter of larger than 10 nm. The electrochemical studies reveal that hydrocarbon products are not favored on nanoparticles less than 15 nm in size. Still, they become increasingly favored as the size grows, which contradicts previous findings by *Manthiram et al.* (**Figure 7f**).[79] It might be due to the difference in dispersion between the two Cu nanoparticles and

the variable thickness of Cu foil. The FE of CH_4 is slightly increased on the 2–20 nm size regime with the high CN increase, indicating the correlation between the FE of CH_4 and the CN of catalysts.

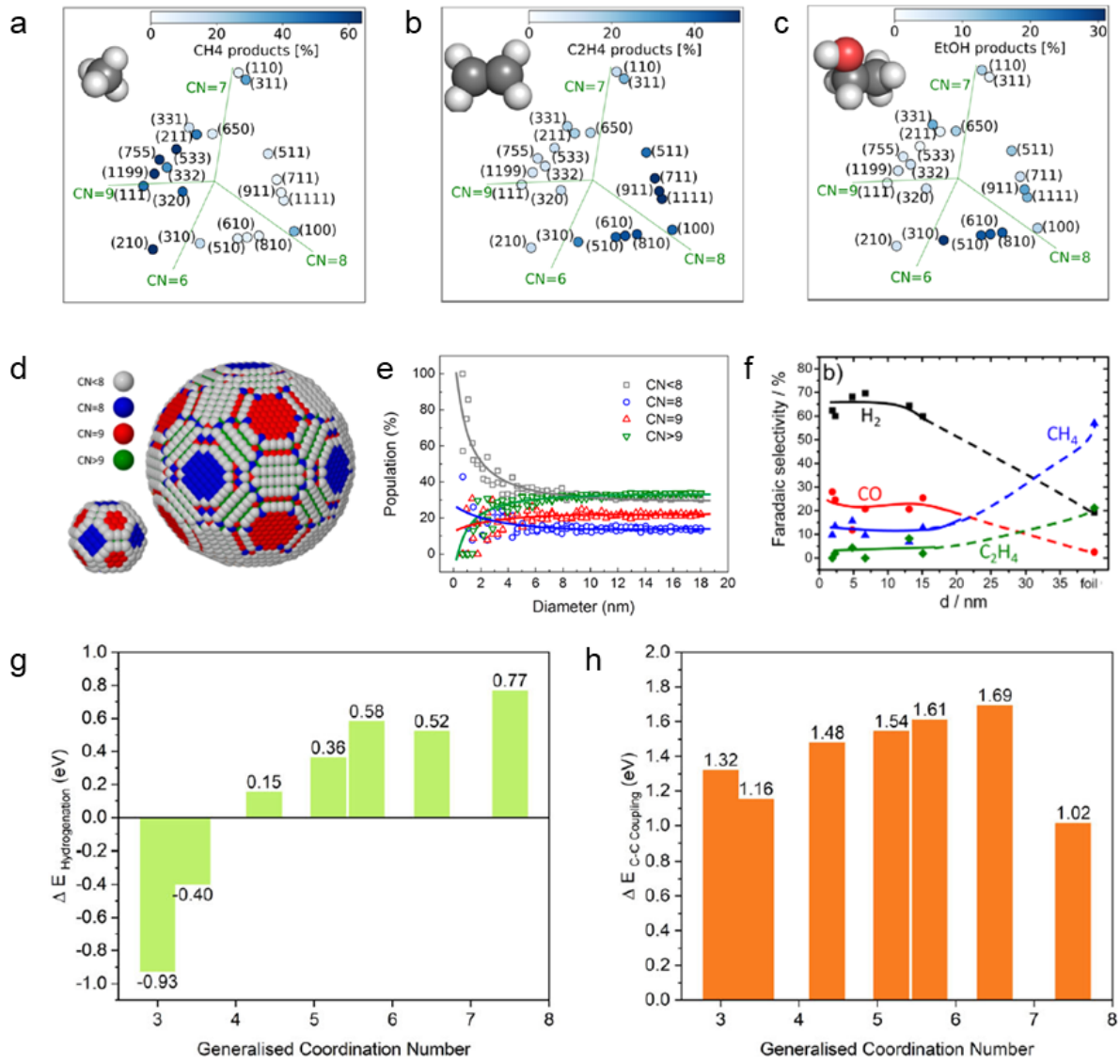

Figure 7. Principal component analysis of the CN allows for the identification of active sites of the Cu catalyst. (a) Cu(111) gives methane, (b) Cu(100) gives ethylene, and (c) the n(100)×(110) step produces ethanol. Reproduced with permission from Rossmeisl *et al.*[89] Copyright 2019 American Chemical Society. (d) Ball models of spherical Cu NPs with diameters of 2.2 and 6.9 nm. (e) Population (relative ratio) of surface atoms with a specific CN as a function of particle diameter. (f) The FE of products during the CO_2RR on Cu nanoparticles. Reproduced with permission from Strasser *et al.*[67] Copyright 2014 American Chemical Society. (g) Reaction energies for *CO hydrogenation to *CHO on Cu catalysts of various generalized CN. (h) Reaction energies for *CO coupling to *OCCO on Cu catalysts of various generalized CN. Reproduced with permission from Sinton *et al.*[90] Copyright 2021 Springer Nature.

Unlike the above finding, it is found that the Cu with a low CN favors the CH_4 formation.[32] It is worth mentioning that the calculation models they used to represent low values of atomic coordination are adparticles configurations. The calculated reaction energies reflect that at the CN of 3.0, the formation of *CHO intermediate (**Figure 7g**) is far more favored than the formation of *OCCO intermediate (**Figure 7h**). The variation in CN has a negligible impact on the C–C coupling process. Thus, the authors believe the low coordination Cu sites can promote CO_2 methanation. They verified this concept by proceeding with the CO_2RR in alkaline electrolytes, not neutral electrolytes, and achieved a FE of 64% for CH_4. Indeed, the CN of active sites greatly influences the performance of CO_2 methanation. As for whether high or low coordination is conducive to methane production, more parameters, such as dispersibility, morphology, and defects, must be considered. As we can see, the CN is related to the facet and the size. Therefore, we should judge the activity of catalysts from many aspects.

2.4 Local pH

The formation of *CHO or *COH from *CO involves the transfer of proton and electron, the so-called concerted proton-electron transfer (CPET) process.[18] In contrast, the *CO dimer formation only involves an electron transfer; thus, it depends on the potential, not the pH. The dependence of CH_4 formation on proton activity suggests that CH_4 production is significantly affected by pH and favored in acidic or neutral solutions.[91] However, as the CO_2 reduction is a proton consumption reaction, the OH^- concentration near the electrode surface increases more than the bulk solution, which increases in the local pH.[92] Thus the electrolyte buffer capacity can regulate the local pH to maintain the local proton concentration in electrolytes with high buffer capacities like phosphate, thereby facilitating the selectivity for CH_4 over C_2H_4.[58] In concentrated $KHCO_3$ or phosphate electrolytes, the produced OH^- can be neutralized by adequate HCO_3^- or $H_2PO_4^-$. Although the CH_4 production is enhanced with high local proton concentration, the HER also would be enhanced. Thus, optimizing the adsorption capacity of electrocatalysts to key intermediates should be considered at the same time.

To achieve an industrially relevant current density of CO_2RR, the alkaline electrolyte is used in a gas-fed flow cell.[93] Using an alkaline electrolyte, the C_2H_4 formation is enhanced, while HER is suppressed and CH_4 formation. Regulating the local pH near the gas diffusion electrode (GDE) is essential for improving the CH_4 selectivity at industrially relevant current densities. A pulsed electrolysis method has been introduced to deplete the OH^- species near the electrode surface to enhance the proton concentration.[94] The pulsed electrolysis conditions are set to 1s pulses at oxidative potentials ranging from E_{an} = 0.6 – 1.5 V_{RHE}, the CO_2RR is proceeded at –0.7 V_{RHE} for 1s. With the

increase of E_{an}, the product selectivity shows a remarkable difference (**Figure 8a**). At E_{an} values below 1.0 V, the yield of CH_4 is negligible. At E_{an} = –1.0 V, the CH_4 product selectivity surge to 25%, and the maximum CH_4 selectivity of 54% can be obtained at E_{an} = –1.5 V. Raman spectra is a surface-sensitive characterization to collect the surface speciation on catalysts (**Figure 8b**). At the potential of –0.7 V, a strong band appeared at 530 cm^{-1}, which is assigned to the Cu-OH signal. Under the pulsed electrolysis conditions, the adsorbed *OH band shows a noticeable decrease with the increase of pulsed potential. The Cu_2O band shows a totally different trend compared to the *OH band, indicating the consumption of OH^- species for Cu_2O formation. The constructed local proton-rich district makes the CH_4 production favorable, achieving a high partial current density of CH_4.

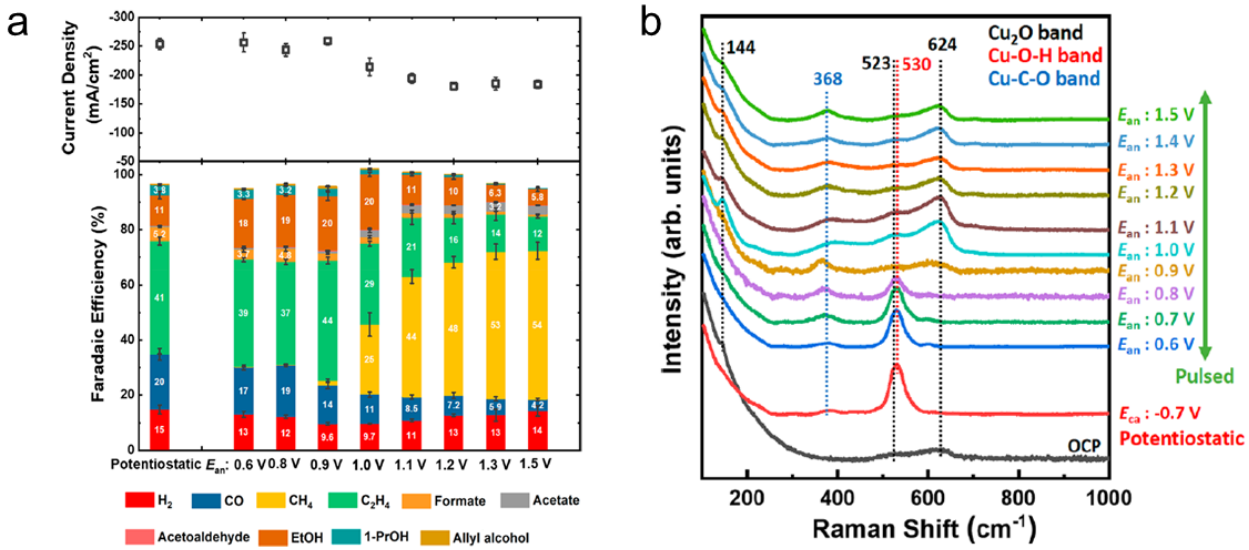

Figure 8. (a) Current density and FE at −0.7 V using potentiostatic and under pulsed electrolysis conditions with the different E_{an} values and the same E_{ca} = −0.7 V cathodic potential in all cases. (b) Operando surface-enhanced Raman spectra under OCP, potentiostatic operation at −0.7 V, and pulsed conditions with different E_{an} values. Reproduced with permission from Cuenya *et al.*[94] Copyright 2021 American Chemical Society.

2.5 Cation/anion effect

The cations or anions in electrolytes play an essential role in the electrochemical reaction since they may interact with the electrode surface, reactants, and intermediates and affect the reaction pathway.[66, 95, 96] The product selectivity of CO_2RR is greatly affected by cationic or anionic species and their concentration. The cation and anion affect the reaction pathway by regulating the surface potential and local pH.[97-99] It is observed that the CH_4 formation increased in the order of Na^+>Li^+>K^+>Cs^+, while the C_2H_4 formation is favorable in the order of Cs^+>K^+>Na^+>Li^+. Because the smaller cation has a larger hydration number and will not be specifically adsorbed on the electrode surface, the extent of specific adsorption of Li^+ would be the least on the surface and that of Cs^+ the

greatest. Specific adsorption of cation shifts the surface potential to the positive direction and lower the H^+ concentration. The pH at the electrode surface will be lower in the $Cs^+>K^+>Na^+>Li^+$ sequence. We have pointed out that the CH_4 formation is favorable in the region with high proton activity. Therefore, the FE of CH_4 is higher in Li^+ and Na^+ solutions, with Na^+ solution being more favorable than Li^+ solution. However, the HER also proceeds in a high H^+ concentration solution simultaneously.

Furthermore, the anions can also affect the local pH by their buffer capacity. The formation of CO, $HCOO^-$, C_2H_4, and CH_3CH_2OH are little affected by the composition and concentration of anions because the rate-limiting step of these products does not involve the H^+.[100] Thus, the anion mainly affects the formation of H_2 and CH_4. Apart from the local pH, anions can affect the surface electronic structure of electrocatalysts; for instance, the halide anions could regulate the catalyst surface electronic structure and thus optimize the reaction pathway.[99] When I- is introduced into the electrolyte, it adsorbs on the Cu surface and donates electrons to Cu, resulting in a negatively charged surface. The interaction between the negatively charged Cu surface and the partially positively charged carbon atom of CO_2 and CO is enhanced (**Figure 9a**), resulting in the enhancement of CO_2 methanation (**Figure 9b**). Therefore, it is obvious that the cations/anions affect the electrochemical properties mainly by regulating the local environment of electrode and electrolyte.

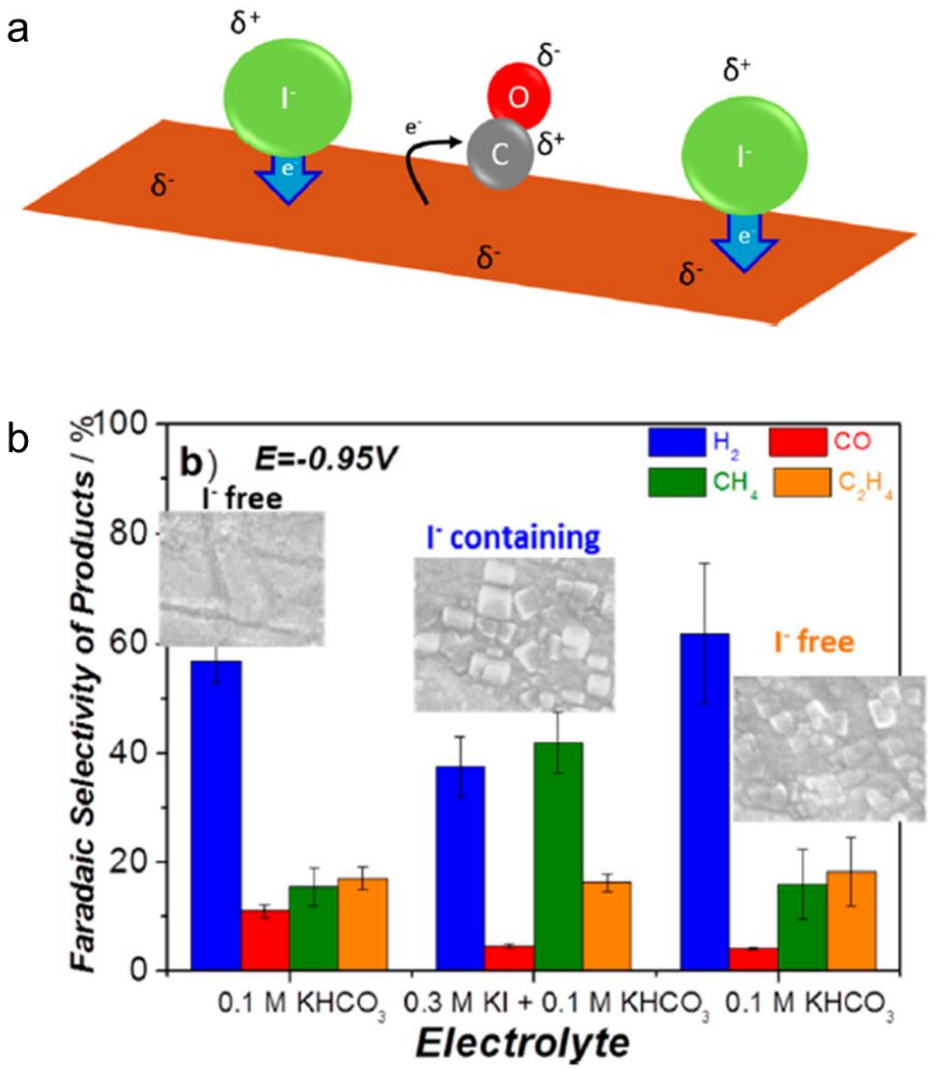

Figure 9. (a) Scheme illustrating how the presence of I^- affects the net charge of Cu, making it more negative and facilitating the charge transfer for CO reduction. (b) Faradaic selectivity of the gaseous products after 10 min of bulk electrolysis at a constant potential of 0.95 V vs. RHE. Including the SEM images of the surface after reaction. Reproduced with permission from Strasser *et al.*[99] Copyright 2016 American Chemical Society.

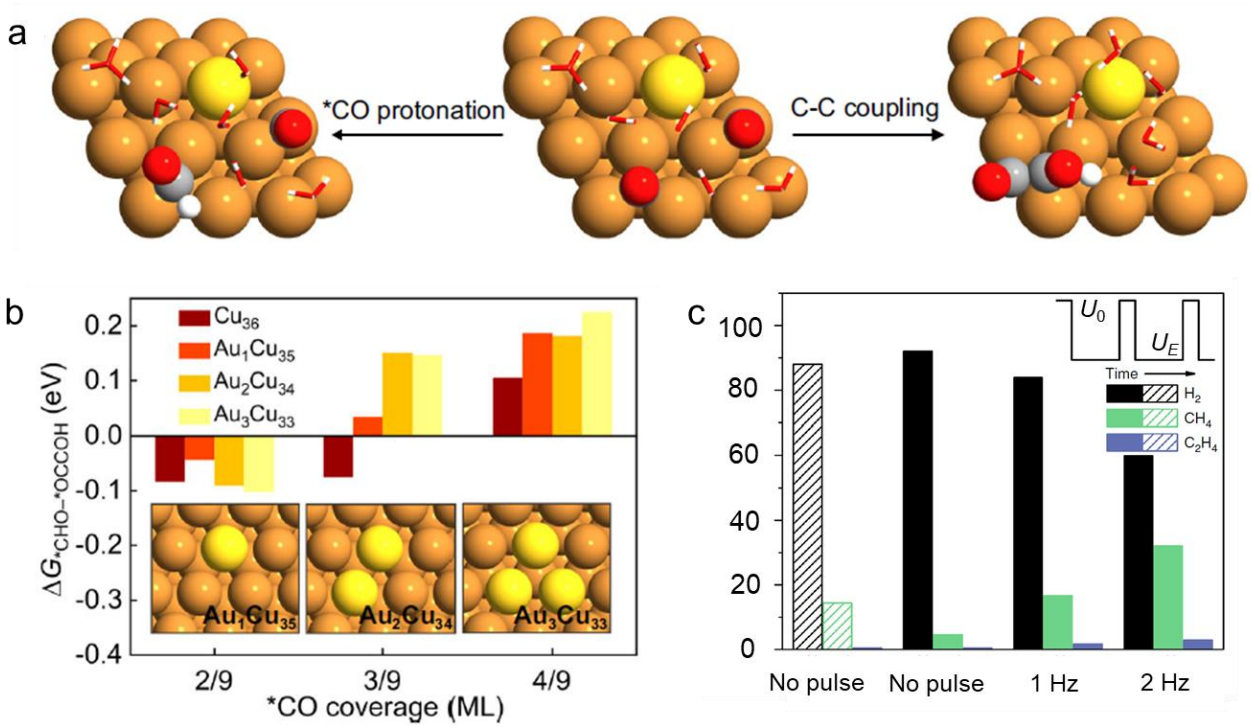

Figure 10. (a) Geometries of *CO, *CHO, and *OCCOH intermediates on Au–Cu surface. (b) Reaction free energy difference between *CO protonation and C–C coupling steps on Cu_{36}, Au_1Cu_{35}, Au_2Cu_{34}, and Au_3Cu_{33} surfaces under different *CO coverages. Reproduced with permission from Sargent *et al.*[101] Copyright 2021 Springer Nature. (c) Faradaic efficiencies of CO electroreduction products with and without square-wave potential electrolysis. Reproduced with permission from Lu *et al.*[102] Copyright 2019 Springer Nature.

2.6 CO concentration

It is important to go through the *CO intermediate phase when producing CH_4 or other C_2 compounds. As a result, it stands to reason that CO concentration influences the reaction pathway and product selectivity.[37, 103-105] Besides, the *CO dimerization and HER should be suppressed to improve the CH_4 selectivity by lowering the surface *CO coverage.[105] DFT studies provide insights into free energies of *CO to *CHO (ΔG_{*CHO}) and C–C coupling (ΔG_{*OCCOH}) for CH_4 production and C_2 products under different *CO coverage to figure out the surface *CO coverage (**Figure 10a**). According to free energy calculations, when the *CO coverage is reduced from 4/9 to 3/9 monolayer the values of ΔG_{*CHO}–ΔG_{*OCCOH} on Cu and Au-Cu surface decrease, which implies that low *CO coverage promotes the CH_4 production (**Figure 10b**). However, using the square-wave potential electrolysis method, after flipping the electrode at a higher frequency, the *CO concentration on the Ag-Cu electrode surface increased, which enhanced the CH_4 selectivity (**Figure 10c**).[104] One consensus is that introducing a CO-producing material on Cu can promote CH_4 production, but the

improved local CO concentration can also promote C_2H_4 generation.[106] Therefore, the *CO concentration cannot be directly correlated with the CH_4 product selectivity.

3. Advanced single sites electrocatalysts towards CO_2 methanation

It is well known that Cu-based catalysts efficiently convert CO_2 into multi-carbon products through C–C coupling pathway. However, when active sites are reduced to single isolated sites, the C–C coupling is inhibited because the two *CO intermediates utilized for C–C coupling is located on two active sites. Thus, C_1 compounds like CO, CH_3OH, and CH_4 are the main products on SSC. To obtain the CH_3OH or CH_4 product, the adsorption of *CO on active sites should be stronger enough so that the *CO can be further reduced and hydrogenated. The coordination structure directly determines the electronic structure of active site, which is essential for the adsorption capacity of SSC to reaction intermediates. In this section, we review the recent advances of the SSC for CO_2 methanation and highlight the coordination structure regulation and reaction mechanism analysis (**Table 1**).

Table 1. Summary of the major SSCs toward methane.

Types	Catalysts	Electrolytes	FE (CH_4)	Current density (CH_4)	Ref.
Molecular SSCs	Cu(I)-based polymer NNU-33 (H)	1 M KOH	82%	391.79 mA cm^{-2}	34
	$Cu_4ZnCl_4(btdd)_3$	0.5 M $NaHCO_3$	88%	18.3 mA cm^{-2}	48
	Cu-TDPP-NS	0.5 M PBS	70%	183 mA cm^{-2}	35
	Cu-DBC	1 M KOH	80%	162.4 mA cm^{-2}	36
	Cu-Tph-COF-Dct	1 M KOH	80%	220 mA cm^{-2}	37
	2Bn-Cu@UiO-67	1 M KOH	81%	340.2 mA cm^{-2}	38
	Plasma activated CuDBC	0.5 M $NaHCO_3$	75.3%	36 mA cm^{-2}	107
	NC-SA Cu/COF	0.1 M $NaHCO_3$	56.2%	4.2 mA cm^{-2}	108
	CoPc@Zn-N-C	1 M KOH	18.3%	44.3 mA cm^{-2}	109

Carbon-supported SSCs	CuN_2O_2	0.5 M $NaHCO_3$	78%	31.2 mA cm^{-2}	47
	Cu SAs/GDY	1 M KOH	81%	243 mA cm^{-2}	39
	Cu SA/F-GDY	1 M KOH	72.3%	174.24 mA cm^{-2}	110
Oxide-supported SSCs	Cu-CeO_2-4%	0.1 M $NaHCO_3$	58%	~36 mA cm^{-2}	111
	Cu/p-Al_2O_3 SAC	1 M KOH	62%	94.8 mA cm^{-2}	46
	Cu/CeO_2	0.1 M $NaHCO_3$	49.3%	~8 mA cm^{-2}	112
	Ir_1−Cu_3N/Cu_2O NCs	1 M KOH	75%	240 mA cm^{-2}	113

3.1 Molecular catalysts

In the early 1980s, nickel and cobalt macrocycles compounds were reported to convert CO_2 into CO.[114] Later on, the application of a series of metal phthalocyanines was explored for CO_2RR and it found that CO is the only product on Co and Ni phthalocyanines.[115] Meanwhile, the formic acid was dominant on Sn, Pd, and In phthalocyanines, methane was the main product on Cu, Ga, and Ti phthalocyanines. However, the molecular catalysts were ignored for decades and applied to CO_2RR recently. A molecular catalyst is a typical SSC that plays an important role in homogeneous and heterogeneous catalysis due to its well-defined and tunable structure.

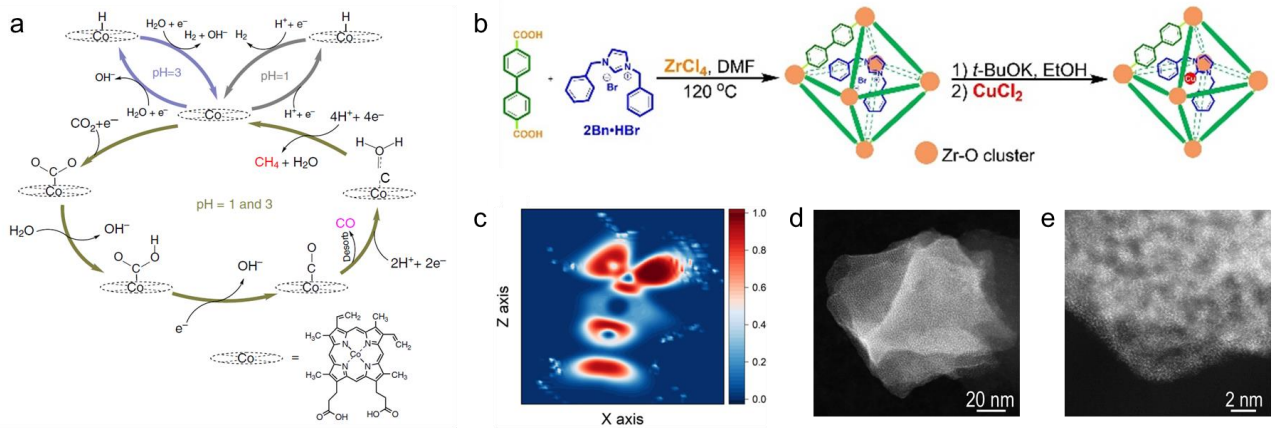

Figure 11. (a) Proposed mechanistic scheme for the electrochemical reduction of CO_2 on Co protoporphyrin. Reproduced with permission from Koper *et al.*[116] Copyright 2015 Springer Nature. (b) The schematic of the synthesis process for 2 Bn-Cu@UiO-67. (c) The electron localization function of the 2Bn-Cu@UiO-67 with the adsorption of *CHO (d-e) HAADF-STEM of 2Bn-Cu@UiO-67. Reproduced with permission from Li *et al.*[38] Copyright 2021 Wiley-VCH GmbH

CO_2 activation is also a decisive step for molecular catalysts to initiate CO_2RR. Because of competing processes such as HER, protons compete with CO_2 for the active site. According to reports, the Co^{2+} in Co protoporphyrin would take an electron to become Co^{+} and then mix with CO_2 to form M-(CO_2^{-}), a Bronsted base capable of attracting protons from water (**Figure 11a**).[33] The CO_2 activation capacity is linked to the Co^{2+}/Co^{+} redox potential; the closer the Co^{2+}/Co^{+} redox potential is to the overall equilibrium potential, the smaller the overpotential for CO2 reduction. However, due to the weak adsorption ability to *CO, the main product on Co protoporphyrin is CO. Thus, a more acidic environment or stronger CO_2/CO adsorption is necessary to reduce the *CO further for higher CH_4 yield. A N-heterocyclic carbene (NHC)-ligated Cu single atom sites embedded into a metal-organic framework (2 Bn-Cu@UiO-67) shows optimized adsorption of *CHO intermediates on the increased charge density of Cu sites due to electron donator effect of NHC ligands (**Figure 11b, c**).[38] Moreover, the porous structure of UiO-67 facilitates the diffusion of CO_2 and enhances mass transfer, yielding a FE of 81% for CH_4 at a high current density of 420 mA cm^{-2} (**Figure 11d-e**). Thus, it is evident that a strong adsorption capacity of a single metal site is essential for further reduction of *CO to CH_4.

Like Co protoporphyrin, Cu^{+} also substantially affects the CO_2 activation and product selectivity in Cu-based molecules. The activity and selectivity of CO_2RR have been demonstrated to be significantly impacted by Cu^{+} in Cu oxides, although Cu^{+} cannot be stabilized in oxides and soon reduces to Cu^{0}.[117] Benefiting from the robust ligand structure, molecular catalysts can stabilize the Cu^{+} active site, where Cu would transform from Cu^{2+} to Cu^{0}. In a non-planar structure molecule, the Cu^{+} can be stabilized by strong trigonal pyramidal coordination (**Figure 12a**). Under CO_2RR condition, the Cu^{2+} sites are reduced to Cu^{+} active sites and stabilize at high-negative potential (**Figure 12b**). Besides, the second coordinate sphere can also stabilize the *CHO intermediates by adjacent aromatic hydrogen atoms, promoting the production of CH_4. For planar structural molecules, introducing coprophilic interactions (Cu–Cu distance in the range of 2.4–3.0 Å) is a feasible strategy to stabilize Cu^{+} sites. A Cu^{+}-based coordination polymer electrocatalyst (**NNU-32**) with abundant coprophilic sites demonstrated an excellent ability of CO_2 to CH_4 conversion.[34]. If a sulfate group is introduced into the molecule (**NNU-32(S)**), the sulfate group will be replaced by a hydroxyl radical (**NNU-32(H)**) in the alkaline electrolyte (**Figure 12c**). The substitution of hydroxyl radicals for sulfate radicals results in enhanced coprophilic interactions and thus further improves the CH_4 product selectivity to 82% at –0.9 V vs. RHE.

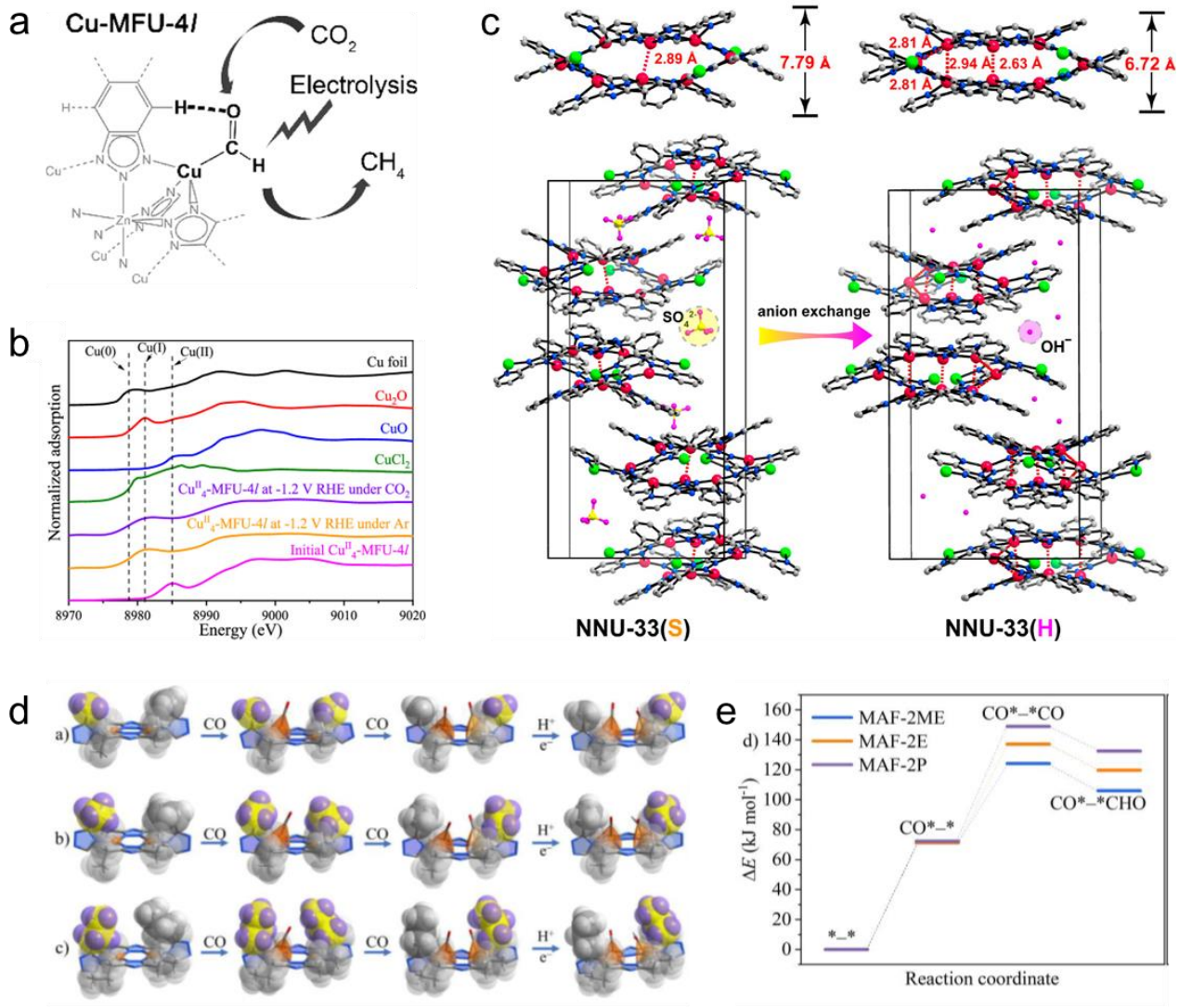

Figure 12. (a) The schematic of CO_2RR mechanism on **Cu-MFU-4*l***. (b) Normalized Cu K-edge XANES spectra of Cu-based samples. Reproduced with permission from Lan *et al.*[48] Copyright 2021 American Chemical Society. (c) The structures of {Cu_8} clusters and unit cell in **NNU-33(S)** and **NNU-33(H)**, respectively. Reproduced with permission from Chen *et al.*[34] Copyright 2021 American Chemical Society. (d) Periodic density functional theory-derived structures of the CO_2RR intermediates for MAF-2ME, MAF-2E, and MAF-2P. (e) Reaction free energies of CO_2RR on MAF-2ME/MAF-2E/MAF-2P. Reproduced with permission from Zhang *et al.*[118] Copyright 2022 Wiley-VCH GmbH.

When designing the coordination structure, it is also necessary to consider the spatial potential resistance effect. The reaction pathway and product selectivity can be successfully modified by varying the size of the second coordination sphere layer ligand. Cu(I) triazolate frameworks with three ligand side groups (MAF-2ME, MAF-2E, and MAF-2P) have been developed, where the steric hindrance prevents the combining of two *CO intermediates as the size of the ligand side groups increases (**Figure 12d**).[118] Thus, the MAF-2P is difficult to distort to bind the second CO intermediate

for producing C_2H_4 (**Figure 12e**). The C_2H_4/CH_4 selectivity ratio can be adjusted from 11.8:1 to 1:2.6 with the size of ligand side groups increasing.

3.2 Carbon-supported catalysts

Carbon-supported metal single atoms catalysts (CS-SAC) have emerged as promising electrocatalysts for CO_2RR. Unlike the single molecular unit of molecule catalysts, CS-SAC has a continuous carbon network with metal atoms embedded in the network, meaning that the coordination structure optimization focuses on the first coordination shell. Metal-N_4-C is a typical structure in CS-SAC, wherea single metal sites possess high stability due to the strong binding strength of N to metal atoms. Cu-based catalysts bear strong adsorption to *CO, so the Cu-based SAC attracts the most attention. To inhibit the possible *CO dimerization, the distance between neighboring Cu-N_x species should be far enough. At a high Cu atom concentration, the distance of two Cu-N_x species was too close to trigger *CO dimerization (**Figure 13a**), and a low Cu atom concentration ensured the high dispersion of Cu-N_x species, favoring the formation of CH_4.[119] At a Cu concentration lower than 2.4%mol, a 38.6% CH_4 FE can be achieved.

Due to possible *CO dimerization on Cu-based SAC, Cu-free SACs are sought for efficient CO_2 conversion into hydrocarbons and oxygenates. Cu-free SACs such as Fe-N_x sites typically convert the CO_2, CO, and CH_2O into CH_4 with a low FE due to the low intrinsic adsorption capacity to *CO with the major products CO (**Figure 13b**).[120] Introducing an axial oxygen atom on M-N_4-C catalysts can change the electronic structure of center metal atoms and affect the adsorption strength of intermediate species.[121] Considering the number of d-electron and electronegativity, five SACs ($Mn{-}N_4{-}C$, $Cr{-}N_4{-}C$, $Os{-}N_4O{-}C$, $Ru{-}N_4O{-}C$, and $Rh{-}N_4O{-}C$) close to the summit of the volcano-shaped relationships between activity descriptor and limiting potentials. But the five-coordination structure is not quite stable. Constructing an oxygen-containing four coordination structure can also promote the further reduction of *CO. A unique Cu-N_2O_2 structure was reported for CO_2 conversion to CH_4 with high selectivity (**Figure 13c**).[47] On Cu-N_2O_2 sites, the overall endothermic energy of intermediates for *COOH and *COH is lower than that of CuN_4 but still higher than that of Cu(111). The enhanced CH_4 selectivity is originated from the higher formation energy of *H adsorption on CuN_2O_2 than that of CuN_4 and Cu(111) because of the optimizing electronic structure (**Figure 13d**). Besides, constructing tandem catalysts is also a feasible pathway to achieve high CH_4 selectivity on Cu-free SAC. Cobalt phthalocyanine (CoPc) is a typical CO-selective catalyst.[122] A CoPc-ZnNC tandem catalyst improves the CH_4/CO production rate ratio by 100 times, with CO_2 first reduced to CO on CoPc sites, then diffused CO reduced to CH_4 through the Langmuir-

Hinshelwood route including an adsorbed *H on Zn sites (**Figure 13e**). It provides an alternative strategy for the possible *CO dimerization in CO_2 methanation.

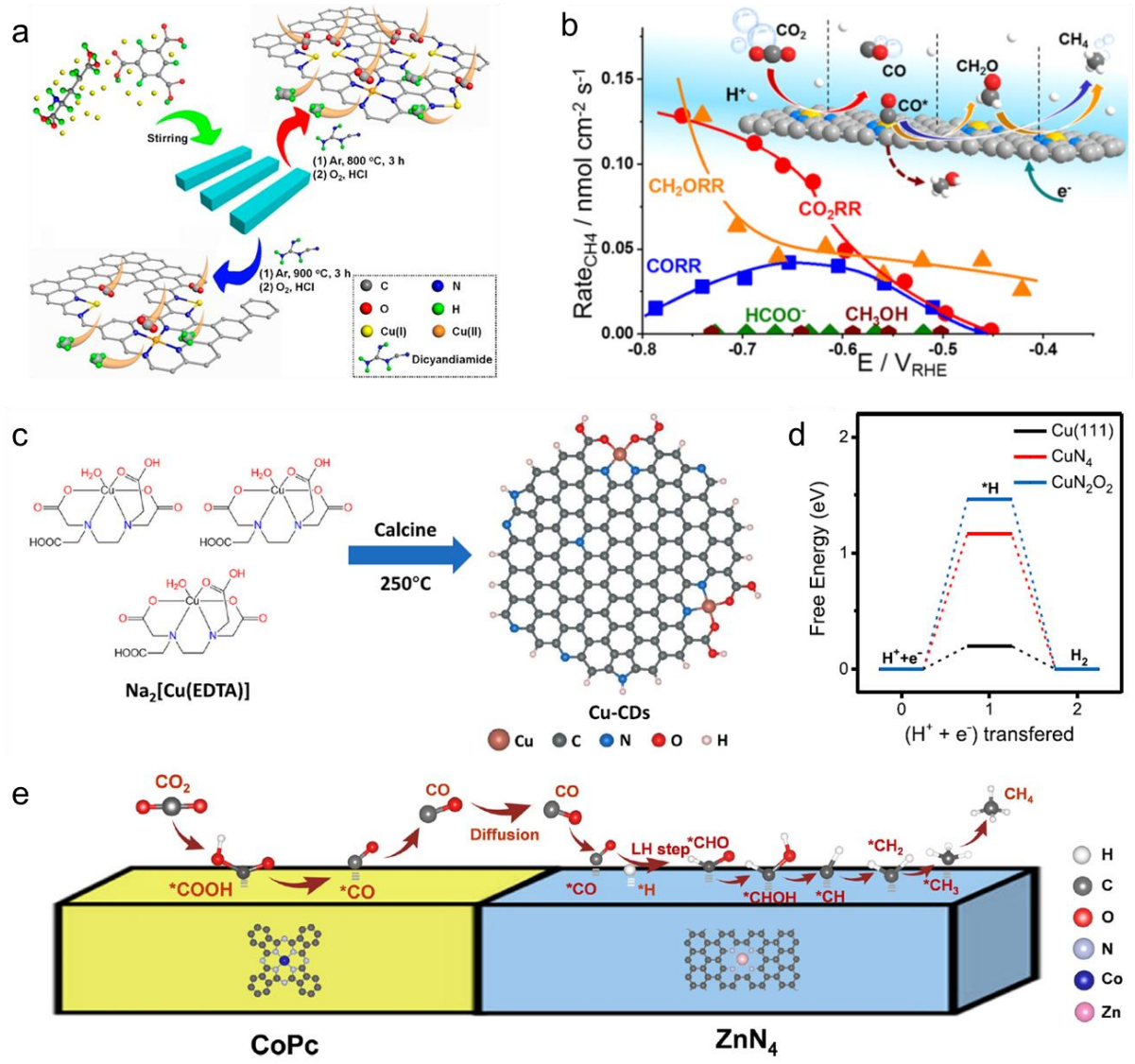

Figure 13. (a) Schematic of the synthesis of the Cu−N−C-T catalysts. (b) Catalytic methane production rate on Fe-N-C during the electrochemical reduction of CO_2, CO, and CH_2O. Reproduced with permission from Strasser *et al.*[120] Copyright 2019 American Chemical Society. (c) Scheme of the synthesis of Cu-CDs (Cu-N_2O_2) catalysts. (d) Free energy diagram of hydrogen evolution on CuN_2O_2, CuN_4, and Cu(111). Reproduced with permission from Zhu *et al.*[123] Copyright 2021 Springer nature. (e) The proposed reaction mechanism of CO_2RR to CH_4 over CoPc@ZnNC. Reproduced with permission from Wang *et al.*[109] Copyright 2020 Wiley-VCH GmbH.

Graphdiyne (GDY) is a unique platform for anchoring single atoms with M-C bonds. The –C≡C–C≡C structure in GDY can stabilize single atoms and trigger electron transfer between the metal center and GDY.[124, 125] On Cu-based SACs-GDY system, the CO_2 methanation may be more easily carried out via the *OCHO pathway to avoid *CO dimerization.[39] The orbital hybridization between the Cu atom and graphite alkyne regulates the electronic structure of the Cu atom, promoting the

valence state of the Cu atom higher than 0. The Cu–C bond also changes the *CO_2 protonation state to *OCHO, which enhances the CH_4 product selectivity.

3.3 Oxide-supported catalysts

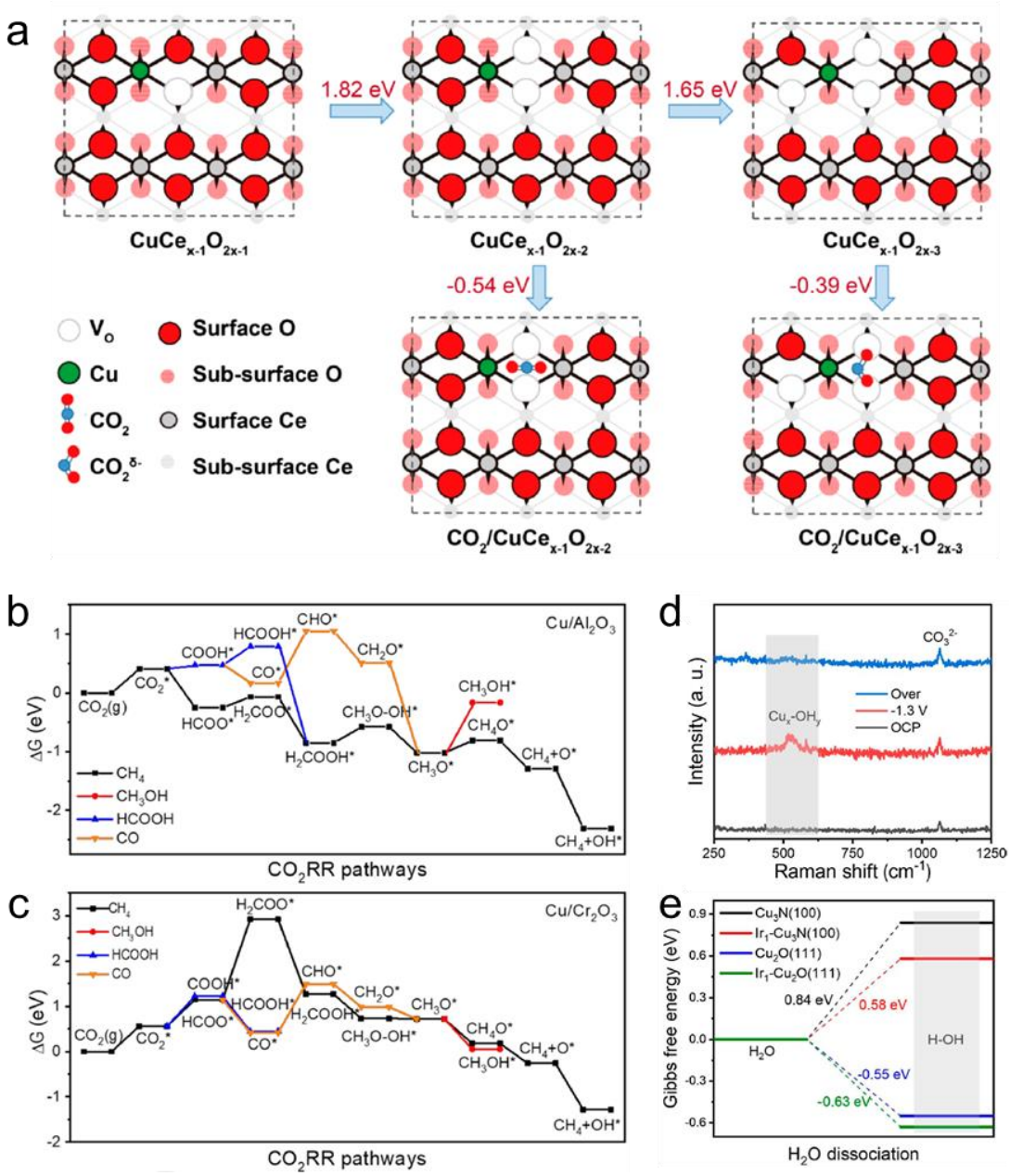

Figure 14. (a) Theoretical calculations of the most stable structures of Cu-doped CeO_2(110) with vacancies and their effects on CO_2 activation. Reproduced with permission from Zheng *et al.*[111] Copyright 2018 American Chemical Society. Calculated free-energy diagrams for the CO_2RR over (b) Cu/Al_2O_3 SAC and (c) Cu/Cr_2O_3 SAC. Reproduced with permission from Li *et al.*[46] Copyright 2021 American Chemical Society. (d) In situ Raman spectrum of Ir1−Cu_3N/Cu_2O. (e) Calculated free energy change for the water dissociation process of Cu_3N(100) and Ir_1−Cu_3N(100) and Cu_2O(111)

and Ir_1−Cu_2O(111). Reproduced with permission from Li *et al.*[113] Copyright 2022 American Chemical Society.

Due to the nature of the vacancy-prone and strong metal-support interactions, metal oxides are widely used to support atomically dispersed metal atoms.[126, 127] Defect-rich metal oxides have strong anchoring capability to metal atoms, which can inhibit the aggregation of metal atoms and *CO dimerization. CeO_2 is known to generate strong metal-support interactions. Au-CeO_x and Ag-CeO_x have shown higher CO FE due to the interface-enhanced effect.[128] Coupling single-atomic Cu substitution and multivacancy can effectively improve the CH_4 selectivity.[111] From theoretical prediction, the structure of three oxygen vacancy (V_O) neighbors to doped Cu atom is the most stable structure (**Figure 14a**). Specifically, the valence state of Cu atoms is reduced to Cu^+ with three V_O, which is more suitable for CH_4 production. The adsorbed CO_2 can be stabilized in a bended structure on the Cu-3V_O site while in linear structure on other vacancies structure or undoped CeO_2. The CO_2 adsorption energy of former structure is –0.39 eV, significantly promoting the CH_4 formation process. As mentioned earlier, a high local proton concentration is beneficial for CO_2 methanation. Apart from the free protons in electrolytes, the Lewis acid-base interactions can also facilitate the stabilization of *HCOO intermediate and CH_4 formation. Chen *et al.*[46] found that loading Cu single atom on strong Lewis acid Al_2O_3 and weak Lewis acid Cr_2O_3 can improve the CH_4 selectivity. On strong Lewis acid Al_2O_3 substrate, the formation energy of *HCOO is only –0.25 eV, far lower than *COOH, and the proton-electron transfer of *CH_3O prefers to produce CH_4 over CH_3OH because of lower free energy increase, which reveals that the CH_4 pathway proceeds preferentially over CO and CH_3OH pathways (**Figure 14b**). When Cu single atoms are loaded on the weak Lewis acid Cr_2O_3, the formation of *HCOO is strongly endothermic (**Figure 14c**). Therefore, the increase of CH_4 formation on Cu/Cr_2O_3 is limited. Benefiting from the strong Lewis acid-base interaction, a high FE of 62% toward CH_4 can be achieved on Cu/Al_2O_3.

In addition to being a reaction active site, metal single atoms can also act as co-catalysts. Chen *et al.*[113] designed an Iridium single-atom doped Cu_3N/Cu_2O hybrid catalysts (Ir_1–Cu_3N/Cu_2O). The Ir_1 is capable of water dissociation to produce H^+ and OH^-. As shown in the results of in-situ Raman (**Figure 14d**), the Cu_x–OH_y species are existed on Ir_1–Cu_3N/Cu_2O when the potential is applied, while it is significantly weak on Cu_3N, indicating the enhancement of water dissociation by introducing Ir_1 atoms. Moreover, the free energy change for water dissociation on Ir_1–Cu_3N (100) (0.58 eV) and Ir_1–Cu_2O (111) (–0.63 eV) deliver smaller absolute value than that of pure Cu_3N (100) (0.84 eV) and Cu_2O (111) (–0.55 eV), further verifying the acceleration of water dissociation by Ir_1 (**Figure 14e**). The Ir_1–Cu_3N/Cu_2O catalysts achieve a high FE of 75% for CH_4 in alkaline flow cells, which is usually unfavorable for CH_4 production. It highlights the importance of designing local coordination environments around active sites. It is worth noting that up to now, most reports on oxides-supported

SACs for CO_2 methanation are based on Cu sites because of the strong adsorption of Cu sites to *CO intermediate. Therefore, more extensive investigations are required for CO_2 methanation on Cu-free oxide-supported SACs.

4. In-situ characterizations for tracing the single active sites

Under the high negative applied potential of CO_2RR, most metal compounds will undergo a decrease in the valence state of the metal ion and a drastic change in the morphology and structure.[113, 129-132] Also, SSCs will undergo obvious changes in the valence state of metal ions, and even restore to zero valences to obtain metal particles or clusters.[133] However, the content of metal atoms in SSCs is usually less than 10 wt%, so it is challenging to trace the structural variation of metal sites during CO_2RR. Thus, in-situ characterizations are crucial in investigating the structural changes of single-site electrocatalysts during CO_2 methanation. These characterizations enable the identification of the active sites and reaction intermediates, as well as the determination of the mechanisms of the catalytic reactions. In-situ techniques such as X-ray absorption spectroscopy (XAS), Raman spectroscopy, infrared spectroscopy, and UV-visible spectroscopy among others, are particularly useful in this regard.[134] By monitoring the changes in the electrocatalyst structure and composition during the reaction, in-situ characterizations provide insights into the reaction mechanism and help to optimize the electrocatalytic performance for CO_2 reduction.

4.1 In-situ XAS

In-situ XAS is a powerful technique used to study the structural changes of materials under electrochemical conditions.[90, 133, 135-137] It involves using synchrotron radiation to probe the electronic and geometric structure of materials. By analyzing the X-ray absorption spectra of the catalyst in real-time during an electrochemical reaction, the oxidation state, coordination geometry, and local environment of the active site of the catalyst can be clearly revealed. XAS encompasses two main methods: X-ray absorption near edge structure (XANES) and extended X-ray absorption fine structure (EXAFS).[138] XANES is a method that provides information on the electronic structure and reveals details about the oxidation state and coordination environment of the atoms in the material. EXAFS, on the other hand, is a technique that provides information on the geometric structure of a material and provides information on the bond distances, coordination numbers, and disorder in a material's structure. In the realm of SSCs, which often contain ultralow amounts of metal, in-situ XAS is a highly effective method for investigating changes in the valence state and coordination structure of the catalyst during electrochemical reactions.

SSCs are typically coordinated to non-metal atoms, most commonly nitrogen atoms, resulting in a tightly bound structure that imparts exceptional stability to these catalysts. However, despite the robust nature of the M-N bonds in SSCs, they can still be disrupted under the extreme conditions of high negative pressure CO_2RR. It has been found that when a single Fe atom exists on Cu(111), it exhibits the strongest affinity for *CO over competing *H and the lowest hydrogenation energy of *CO, indicating a propensity for CO_2RR to produce methane (**Figure 15a**).[135] As the size of the Fe unit increases from single atoms to nanoparticles, the selectivity of CO_2RR products decreases, while that of H_2 increases, owing to the highest affinity of single-site Fe for *CO over *H. Preventing the aggregation of single-site Fe during CO_2RR is crucial. Fe single atoms in Fe phthalocyanine (FePc) are well-isolated, with a significant distance between two Fe single atoms. The Fe single atom can be maintained by anchoring FePc units onto Cu(111) even if Fe^{2+} is reduced to Fe^0. Through in-situ XAS analysis, it has been discovered that during CO_2RR, the Fe-N bond dissociates, and a Fe-Cu metallic bond emerges, with a lower coordination intensity than pure Fe metal (**Figure 15b**). As a result, the oxidation state shifts from a cation to a metallic state, and the electronic state differs from that of pure Fe metal (**Figure 15c**). The significant diameter of the phthalocyanine ring (15 Å) effectively isolates iron ions (2.52 Å) and prevents the self-aggregation of Fe ions.

Cu-N based SCCs are the most common catalysts for CO_2 methanation. However, it is reported that a Cu-N-C material composed of predominantly Cu-N sites can catalyze CO_2 into ethanol with high faradaic efficiency.[136, 139] As we all know, the formation of C_2 product involves two *CO intermediates on two active sites nearby and the large interatomic distances of single sites would not allow this process to occur (**Figure 15d**).[140] Therefore, when C_2 products are observed, cluster formation is highly probable. Using ex-situ characterizations such as X-ray photoelectron spectroscopy (XPS) and high-angle annular darkfield scanning transmission electron microscopy (HAADF-STEM), it is found that the Cu-N_4 motifs can be maintained post-electrolysis, which prompted us to consider whether there is a different reaction mechanism. However, in-situ XAS showed that the Cu^{2+} reduction to Cu^0 and Cu-Cu coordination showed up below –0.6 V vs. RHE, indicating the formation of Cu clusters during the CO_2 electrolysis. Interestingly, after exposure to air for 10 hours or applying a positive potential of +1 V vs. RHE, Cu-Cu coordination disappeared while the original Cu-N coordination recovered. These results suggest that the Cu_n clusters produced during electrolysis are responsible for the ethanol production and the Cu-N structure can be recovered with the oxidation of Cu^0 because the undercoordinated N sites still exist, which would catch the metal ions (**Figure 15e**). Different Cu single site coordination structures are transformed into clusters of various sizes during the CO_2RR, which significantly impacts on the regeneration of their structures. A typical Cu-based molecular catalyst, copper(II) phthalocyanine (CuPc), reversibly restructure to Cu clusters with a size of ~2 nm upon application and release of negative electrode potential.[133] In

contrast, in a Cu-O coordinated metal-organic framework (MOF), copper(II) benzene-1,3,5-tricarboxylate (btc) MOF (HKUST-1) irreversibly decomposes to form much larger Cu nanostructures. As shown in the fitting results of in-situ EXAFS (**Figure 15f-h**), the Cu-N and Cu-O coordination decrease quickly while the Cu-Cu coordination gradually increases with the decrease of potential. As the applied potential is switched back to 0.64 V vs. RHE, the Cu-N coordination dominates the spectrum again, indicating the regeneration of CuPc. The coordination number of Cu-Cu increase obviously after –0.76 V vs. RHE and obtain a coordination number of 6.5 around –1.1 V vs. RHE, corresponding to the highest CH_4 FE of 66%, suggesting a suitable coordination number for CO_2 methanation.

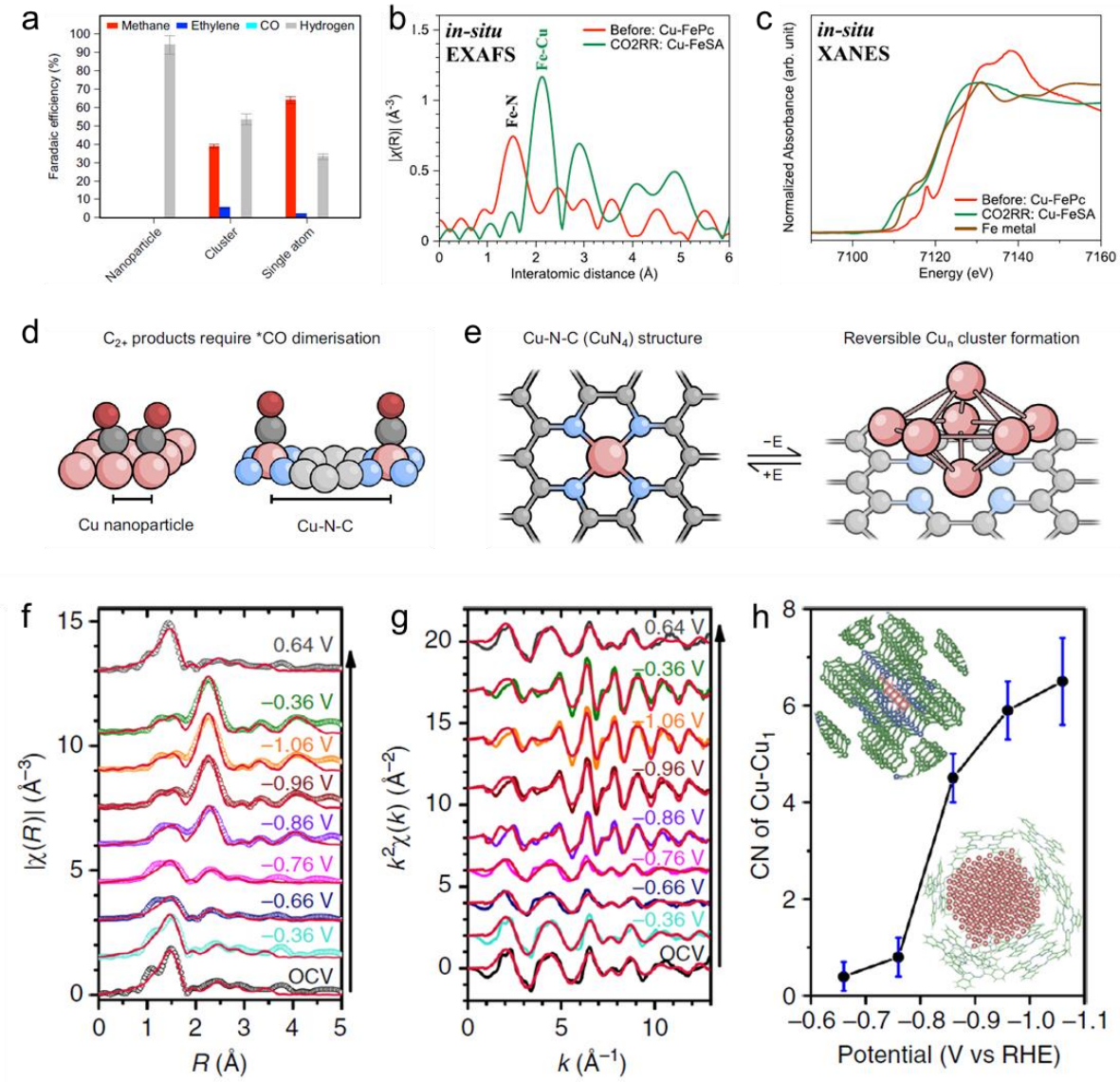

Figure 15. (a) The FE of CH_4 on various iron-dispersed copper materials, including nanoparticle, cluster, and single-atom forms. (b) In-situ EXAFS and (c) XANES of Fe K-edge for Cu-FeSA during CO_2RR. Reproduced with permission from Sargent *et al.*[135] Copyright 2022 Springer nature. (d) Illustration of how Cu-Cu distances affect the *CO dimerization. (e) Schematic showing the formation of Cu_n clusters under applied cathodic potential and the reversibility under oxidative

potentials. Reproduced with permission from Fontecave *et al.*[140] Copyright 2022 Springer nature. Fitted (f) R-space and (g) k-space EXAFS spectra of the CuPc catalyst. (h) First-shell Cu–Cu CNs of the CuPc catalyst at different potentials. Reproduced with permission from Wang *et al.*[133] Copyright 2018 Springer nature.

4.2 In-situ Raman spectroscopy

In-situ Raman spectroscopy is an effective technique for studying the catalysts structure and reaction intermediates iduring CO_2RR.[141-143] Raman spectroscopy involves the analysis of the inelastic scattering of light, providing information about the vibrational modes and molecular structure of the species present in a system. In-situ Raman spectroscopy allows for real-time monitoring of the reaction intermediates and products, but is not commonly used in CO_2 reduction because of the particularly low intermediates concentration. The signal of intermediates can be clearly detected unless metals with surface enhancement effects, such as Au, Ag, Cu, are introduced.[144] Additionally, in-situ Raman spectroscopy enables the investigation of catalyst dynamics and structural changes during CO_2 reduction. It can reveal alterations in the catalyst surface, such as changes in surface roughness, restructuring of active sites, or the formation of reaction byproducts that may affect catalyst performance. For SSCs, we can track the valence reduction of metal center during the CO_2RR, which have a great effect on the adsorption to CO_2. Using in-situ/operando Raman spectroscopy, Ren et al. confirmed that the Co center of CoPc was the active site at high currents and more electron at the Co^I center can increase the CO formation rates (**Figure 16a**).[145] Both Co^{II} and Co^I oxidation states provide diagnostic Raman signatures near 760 and 1140 cm^{-1} in Raman spectra It is reported that the low conductivity may cause the aggregation of catalytic sites because of the electronic isolation, resulting in the coexistence of active Co^I sites and inactive Co^{II} sites.[146] With low CoPc loading of $1.9 \pm 0.5 \times 10^{-7}$ mol cm^{-2} on GDE, during CO_2RR, a ratio of ~1:1.35 for Co^I and Co^{II} sites was determined and the primary gaseous product was CO with low partial current density and high turnover frequency (**Figure 16b**). At a high CoPc loading of $9.2 \pm 0.5 \times 10^{-7}$ mol cm^{-2}, the CoPc show more aggregated micrometer-sized particles on GDE and Co^{II} become the dominant species during CO_2RR (**Figure 16c**). The low CO partial current density and low turnover frequency indicate that the increased CoPc was aggregated and does not contribute to the CO_2 conversion. By introducing porous carbon nanoparticles (CNP) with low CoPc loading of $1.9 \pm 0.5 \times 10^{-7}$ mol cm^{-2} onto GDE to reduce the aggregation of CoPc, high CO partial current density and high turnover frequency can be achieved. Operando Raman spectroscopy revealed the percentage of 91.5% for Co^I during CO_2RR (**Figure 16d**). These results suggest that dispersing molecular catalysts on conductive matrix is necessary to ensure the exposure of active sites.

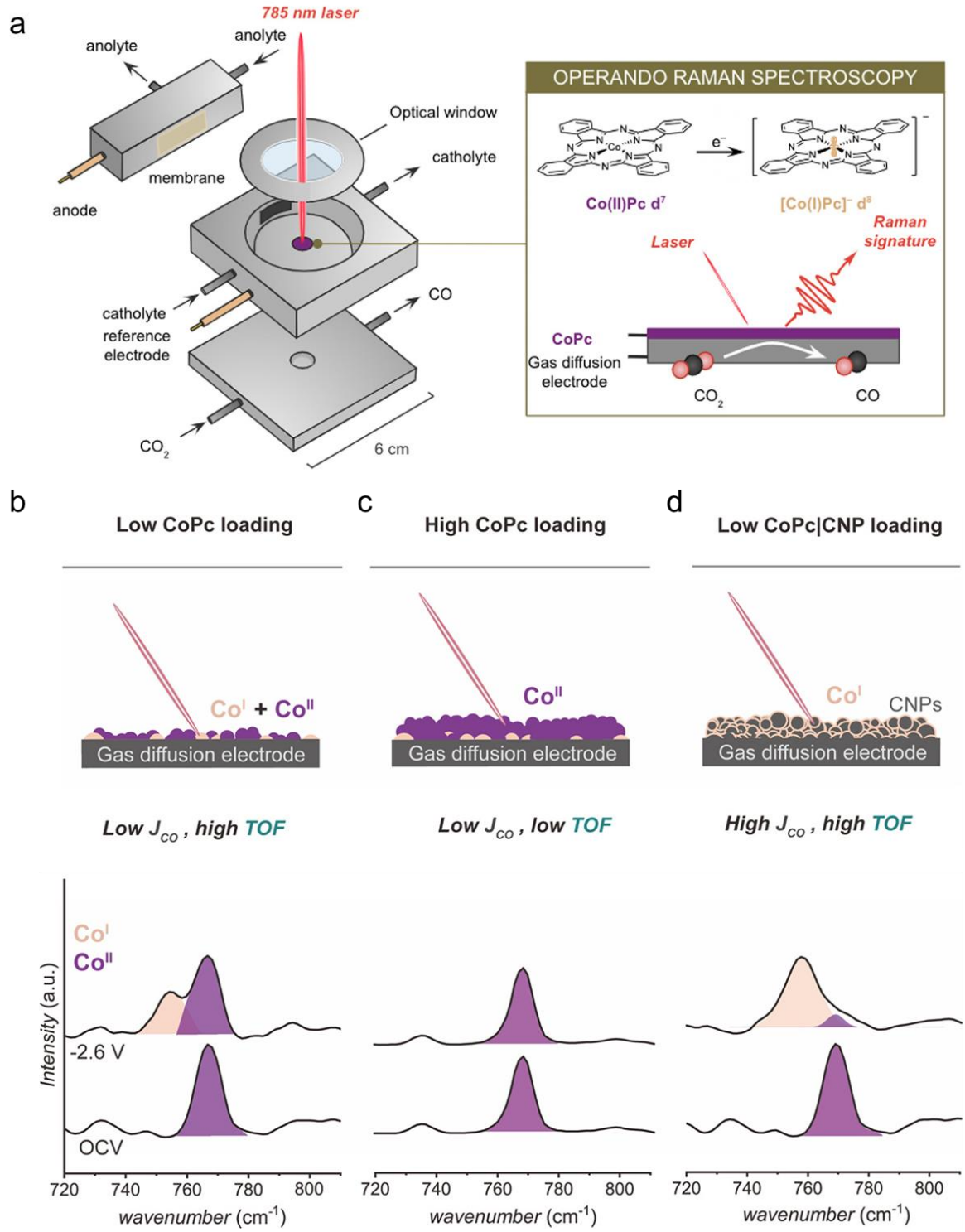

Figure 16. (a) Operando Raman spectroscopy electrochemical flow cell for operando detection of active sites variation in immobilized molecular electrocatalysts. The distribution of Co^{I} and Co^{II} sites in CoPc molecular catalysts determined by operando Raman spectroscopy for (b) low CoPc loading, (c) high CoPc loading, and (d) low CoPc/CNP loading. Reproduced with permission from Berlinguette *et al.*[145] Copyright 2023 American Chemical Society.

4.3 In-situ UV-visible spectroscopy

In-situ UV-visible spectroscopy is a powerful technique used to investigate the electronic properties and structural changes of catalysts under various conditions. It can be used to study the kinetics and dynamics of reactions, monitor changes in the catalyst's oxidation state, and investigate the stability and degradation of catalyst materials over time. The in-situ UV-visible spectroscopy is well suited to the SSCs, especially the molecular catalysts like metal phthalocyanine, because the molecular groups have strong adsorption capacity. The working electrode is obtained by depositing catalysts on a transparent platinum sputtered quartz plate, and all the electrode and gas tube are inserted into a standard quartz cell (**Figure 17a**).[123] As discussed in the results of in-situ XAS, the CuPc would convert into metallic Cu clusters under CO_2RR and convert back to CuPc upon release of the reduction potential. Using in-situ UV-visible spectroscopy, the decomposition and recovery of CuPc was also confirmed. As shown in **Figure 17b**, the reduction of CuPc and the rising absorption of Pc can be observed, corresponding to the formation of Cu^+ and Cu^0. When the working potential returned to OCP, the adsorption of CuPc showed up again. For a carbon dots-supported Cu-N_2O_2 single sites catalyst (Cu-CDs), decreasing electrode potential did not show variation during CO_2RR (**Figure 17c**), indicating the intrinsic activity of Cu center and the stability of the Cu-N_2O_2 coordination structure.

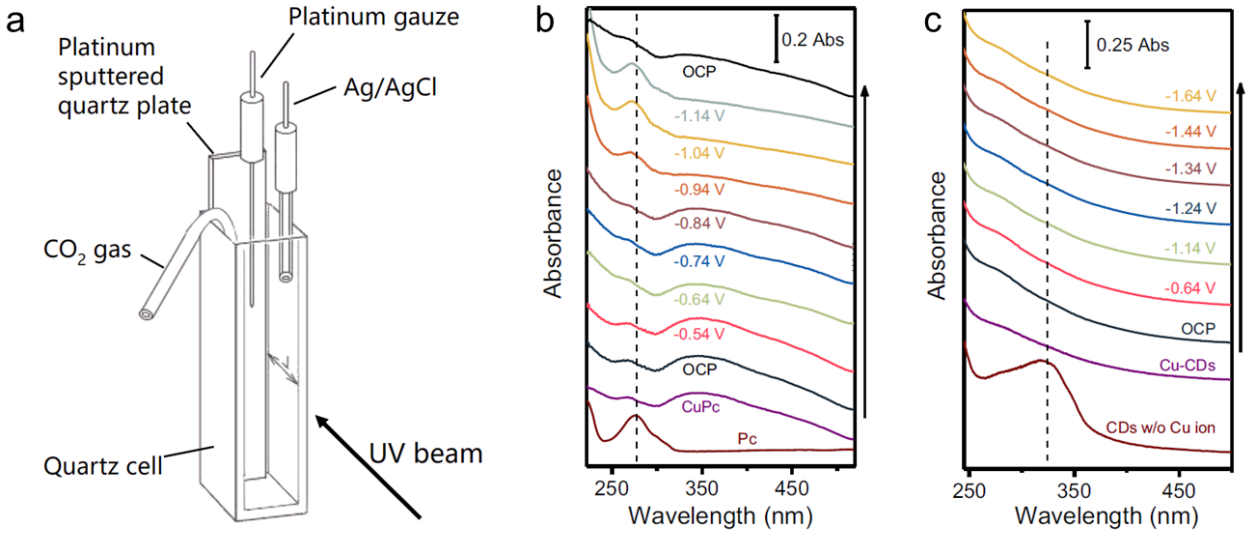

Figure 17. (a) Schematic illustration of the in-situ UV–visible spectroscopy setup. In-situ UV-visible spectra of (b) CuPc, and (c) Cu-CDs. Reproduced with permission from Zhu *et al.*[123] Copyright 2021 Springer nature.

The options for in-situ characterization of single-site catalysts for structure tracking are limited. In-situ XAS is considered one of the most effective techniques which provides valuable information about the electronic and geometric structure of the SSCs during catalytic reactions. However, it is true that the availability of synchrotron light sources, which are necessary for performing in-situ XAS

experiments, limit the laboratory-scale testing of SSCs. Nonetheless, efforts are being made to develop alternative laboratory-based X-ray sources, such as benchtop X-ray absorption spectroscopy instruments, which could potentially broaden the accessibility of in-situ XAS experiments for SSCs. Additionally, the development of alternative in-situ characterization techniques for tracking the structural changes of SSCs is of great importance. Diversifying the range of available methods can provide complementary insights into the dynamic behavior of SSCs during catalytic reactions. By exploring and advancing other in-situ characterization techniques, researchers can broaden their understanding of SSCs and their structural transformations, paving the way for improved catalyst design and performance optimization.

5. Conclusions and perspectives

This review presents the first comprehensive discussion of the reaction mechanism, activity descriptors, and catalyst design for electrochemical CO_2 methanation over single-site catalysts. Firstly, the factors affecting the catalytic activity of CO_2 methanation are discussed, mainly the ligand environment, including the catalyst ligand structure and the reaction environment. In conjunction with the ligand structure design, we detail three main types of single-site catalysts for CO_2 methanation. Most Cu-based catalysts are obviously more competent in adsorbing intermediate products and achieving multi-electron transfer. Appropriate ligand structure design can effectively inhibit the formation of multi-carbon products on copper-based SSCs, thus improving the selectivity of methane. So far, CO_2 methanation over SSC has achieved high selectivity. Still, its current density, turnover frequency, and stability performance have not yet met the requirements of large-scale operation for industrialization. The option of in-situ characterizations also limits the investigation of the dynamic changes of active sites. In this regard, the following several potential perspectives could be helpful for SSCs to achieve industrial CO_2 methanation.

1) *Developing non-Cu-based SSC*. Cu-based catalysts reduce CO_2 well but have poor single-product selectivity. On the other hand, other metal catalysts are more selective for C_1 products, although obtaining methane from CO_2 is challenging. Although the single-site copper catalysts can inhibit the formation of C_2 products, the catalyst reconfiguration during the reaction may still lead to the emergence of Cu particulate species, resulting in increased C_2 product selectivity. Therefore, a more feasible route is optimizing non-Cu-based single-site catalysts for near 100% selective methane production.

2) *Developing characterization technology with higher spatial and temporal resolution*. The SSCs exhibit different structural stability with different coordination structure. The single metal sites coordinated with O/N are incredibly stable, while the metal-N_4 structure quickly transform to metal

monomers under bias. Similarly, the CO_2RR performance on nanoparticles varies considerably as compared to SSCs. Therefore, more in-situ characterizations should be developed to establish the relationship between coordination structure and performance than just in-situ XAS and in-situ Raman.

3) *Preparing high mass-loading SSC*. SSCs with high mass loading are required for industrial applications, yet developing SSCs with mass loading of more than 5% remains a significant challenge. Therefore, coordination and morphology structure should be appropriately designed to ensure high mass loading and the full exposure of active sites.

4) *CO_2 methanation in acidic electrolytes*. Although CO_2 methanation is more likely to occur in a proton-rich environment, practically all studies in the present literature are based on neutral and simple media. The fact that the HER is extremely active in acidic electrolytes is another significant challenge. Besides, suppose CO_2 occupies the single active site in SSCs. In that case, the protons cannot be adsorbed on active sites, which limits the HER and efficient CO_2 methanation can be achieved in acidic electrolytes. Therefore, it is vital to regulate the coordination environment of single active sites to enhance the capacity of active sites for CO_2 adsorption than the proton.

5) *Developing CO_2-CO-CH_4 tandem system*. CO is an important intermediate for CO_2 methanation. The CO selectivity close to 100% is achieved on many kinds of SSCs. Thus, developing a system that involves the conversion of CO_2 into CO and then further into methane CH_4 on different cell system may help stabilizing *CO intermediate and promote the protonation process.

6) *The industrial application of electrochemical CO_2 methanation*. Although CO_2 methanation holds promise as an environmentally friendly solution for converting CO_2 emissions into a useful energy source, thus contributing to a reduction in greenhouse gas emissions. However, on an industrial scale, the resulting methane gas must be stored in a controlled manner to prevent its leakage from making the greenhouse effect worse. At the same time, the utilization rate of CO_2 also deeply affects whether the process is environmentally friendly. Ensuring the durability of the electrochemical cells and systems used in this process is vital for minimizing maintenance costs and maximizing the lifespan of the equipment. In addition to these, widespread adoption of this technology in various industries may require incentivizing policies and public awareness campaigns to encourage its use.

Acknowledgements

L.M. acknowledges the National Key Research and Development Program of China (2020YFA0715000), National Natural Science Foundation of China (51832004,52127816), National Energy-Saving and Low-Carbon Materials Production and Application Demonstration Platform Program (TC220H06N). S.C. acknowledge the “Young Talent Support Plan” of Xi'an Jiaotong University.

Conflict of Interest

The authors declare no conflict of interest.

References

1. P. De Luna, C. Hahn, D. Higgins, S. A. Jaffer, T. F. Jaramillo and E. H. Sargent, *Science*, 2019, **364**, eaav3506.
2. O. S. Bushuyev, P. De Luna, C. T. Dinh, L. Tao, G. Saur, J. van de Lagemaat, S. O. Kelley and E. H. Sargent, *Joule*, 2018, **2**, 825-832.
3. A. Ozden, F. P. García de Arquer, J. E. Huang, J. Wicks, J. Sisler, R. K. Miao, C. P. O'Brien, G. Lee, X. Wang and A. H. Ip, *Nat. Sustain.*, 2022, **5**, 563–573.
4. M. G. Kibria, J. P. Edwards, C. M. Gabardo, C. T. Dinh, A. Seifitokaldani, D. Sinton and E. H. Sargent, *Adv. Mater.*, 2019, **31**, 1807166.
5. O. Hoegh-Guldberg, D. Jacob, M. Taylor, T. Guillén Bolaños, M. Bindi, S. Brown, I. A. Camilloni, A. Diedhiou, R. Djalante and K. Ebi, *Science*, 2019, **365**, eaaw6974.
6. Y. Quan, J. Zhu and G. Zheng, *Small Sci.*, 2021, **1**, 2100043.
7. J. E. Huang, F. Li, A. Ozden, A. Sedighian Rasouli, F. P. García de Arquer, S. Liu, S. Zhang, M. Luo, X. Wang and Y. Lum, *Science*, 2021, **372**, 1074-1078.
8. Y. Li, A. Ozden, W. R. Leow, P. Ou, J. E. Huang, Y. Wang, K. Bertens, Y. Xu, Y. Liu and C. Roy, *Nat. Catal.*, 2022, **5**, 185-192.
9. J. Wicks, M. L. Jue, V. A. Beck, J. S. Oakdale, N. A. Dudukovic, A. L. Clemens, S. Liang, M. E. Ellis, G. Lee and S. E. Baker, *Adv. Mater.*, 2021, **33**, 2003855.
10. Z. Zhang, E. W. Lees, F. Habibzadeh, D. A. Salvatore, S. Ren, G. L. Simpson, D. G. Wheeler, A. Liu and C. P. Berlinguette, *Energ. Environ. Sci.*, 2022, **15**, 705-713.
11. S. Nitopi, E. Bertheussen, S. B. Scott, X. Liu, A. K. Engstfeld, S. Horch, B. Seger, I. E. L. Stephens, K. Chan and C. Hahn, *Chem. Rev.*, 2019, **119**, 7610-7672.
12. S. Navarro-Jaén, M. Virginie, J. Bonin, M. Robert, R. Wojcieszak and A. Y. Khodakov, *Nat. Rev. Chem.*, 2021, **5**, 564-579.

13. Y. Wang, Y. Zheng, C. Han and W. Chen, *Nano Res.*, 2021, **14**, 1682-1697.

14. P. Zhu, X. Xiong and D. Wang, *Nano Res.*, 2022, **15**, 5792-5815.

15. H. Jing, P. Zhu, X. Zheng, Z. Zhang, D. Wang and Y. Li, *Adv. Powder Mater.*, 2022, **1**, 100013.

16. J. Zhu, J. Li, R. Lu, R. Yu, S. Zhao, C. Li, L. Lv, L. Xia, X. Chen and W. Cai, *Nat. Commun.*, 2023, **14**, 4670.

17. W. Zong, H. Gao, Y. Ouyang, K. Chu, H. Guo, L. Zhang, W. Zhang, R. Chen, Y. Dai and F. Guo, *Angew. Chem. Int. Edit.*, 2023, **135**, e202218122.

18. Y. Y. Birdja, E. Pérez-Gallent, M. C. Figueiredo, A. J. Göttle, F. Calle-Vallejo and M. Koper, *Nat. Energy*, 2019, **4**, 732-745.

19. S. Verma, S. Lu and P. J. A. Kenis, *Nat. Energy*, 2019, **4**, 466-474.

20. S. Zhang, Q. Fan, R. Xia and T. J. Meyer, *Acc. Chem. Res.*, 2020, **53**, 255-264.

21. Z. Zhang, J. Zhu, S. Chen, W. Sun and D. Wang, *Angew. Chem. Int. Edit.*, 2022, **62**, e202215136.

22. A. Caballero and P. J. Perez, *Chem. Soc. Rev.*, 2013, **42**, 8809-8820.

23. L. Sun, Y. Wang, N. Guan and L. Li, *Energy Technol.*, 2020, **8**, 1900826.

24. M. Younas, L. Loong Kong, M. J. K. Bashir, H. Nadeem, A. Shehzad and S. Sethupathi, *Energy Fuels*, 2016, **30**, 8815-8831.

25. S. Kattel, P. Liu and J. G. Chen, *J. Am. Chem. Soc.*, 2017, **139**, 9739-9754.

26. C. Vogt, E. Groeneveld, G. Kamsma, M. Nachtegaal, L. Lu, C. J. Kiely, P. H. Berben, F. Meirer and B. M. Weckhuysen, *Nat. Catal.*, 2018, **1**, 127-134.

27. R.-P. Ye, J. Ding, W. Gong, M. D. Argyle, Q. Zhong, Y. Wang, C. K. Russell, Z. Xu, A. G. Russell and Q. Li, *Nat. Commun.*, 2019, **10**, 5698.

28. R. Kortlever, J. Shen, K. J. P. Schouten, F. Calle-Vallejo and M. T. M. Koper, *J. Phys. Chem. L*, 2015, **6**, 4073-4082.

29. K. J. P. Schouten, Z. Qin, E. Pérez Gallent and M. T. M. Koper, *J. Am. Chem. Soc.*, 2012, **134**, 9864-9867.

30. K. J. P. Schouten, Y. Kwon, C. J. M. Van Der Ham, Z. Qin and M. T. M. Koper, *Chem. Sci.*, 2011, **2**, 1902-1909.

31. R. Zhao, P. Ding, P. Wei, L. Zhang, Q. Liu, Y. Luo, T. Li, S. Lu, X. Shi and S. Gao, *Adv. Funct. Mater.*, 2021, **31**, 2009449.

32. Y. Xu, F. Li, A. Xu, J. P. Edwards, S.-F. Hung, C. M. Gabardo, C. P. O'Brien, S. Liu, X. Wang and Y. Li, *Nat. Commun.*, 2021, **12**, 1-7.

33. J. Shen, R. Kortlever, R. Kas, Y. Y. Birdja, O. Diaz-Morales, Y. Kwon, I. Ledezma-Yanez, K. J. P. Schouten, G. Mul and M. Koper, *Nat. Commun.*, 2015, **6**, 1-8.

34. L. Zhang, X.-X. Li, Z.-L. Lang, Y. Liu, J. Liu, L. Yuan, W.-Y. Lu, Y.-S. Xia, L.-Z. Dong and D.-Q. Yuan, *J. Am. Chem. Soc.*, 2021, **143**, 3808-3816.

35. Y. R. Wang, M. Liu, G. K. Gao, Y. L. Yang, R. X. Yang, H. M. Ding, Y. Chen, S. L. Li and Y. Q. Lan, *Angew. Chem. Int. Edit.*, 2021, **60**, 21952-21958.

36. Y. Zhang, L.-Z. Dong, S. Li, X. Huang, J.-N. Chang, J.-H. Wang, J. Zhou, S.-L. Li and Y.-Q. Lan, *Nat. Commun.*, 2021, **12**, 1-9.

37. Y. R. Wang, H. M. Ding, X. Y. Ma, M. Liu, Y. L. Yang, Y. Chen, S. L. Li and Y. Q. Lan, *Angew. Chem. Int. Edit.*, 2022, **61**, e202114648.

38. S. Chen, W. H. Li, W. Jiang, J. Yang, J. Zhu, L. Wang, H. Ou, Z. Zhuang, M. Chen and X. Sun, *Angew. Chem. Int. Edit.*, 2022, **61**, e202114450.

39. G. Shi, Y. Xie, L. Du, X. Fu, X. Chen, W. Xie, T. B. Lu, M. Yuan and M. Wang, *Angew. Chem. Int. Edit.*, 2022, **61**, e202203569.

40. L. Xiong, X. Zhang, L. Chen, Z. Deng, S. Han, Y. Chen, J. Zhong, H. Sun, Y. Lian and B. Yang, *Adv. Mater.*, 2021, **33**, 2101741.

41. Y.-L. Qiu, H.-X. Zhong, T.-T. Zhang, W.-B. Xu, X.-F. Li and H.-M. Zhang, *ACS Catal.*, 2017, **7**, 6302-6310.

42. J. D. Yi, R. Xie, Z. L. Xie, G. L. Chai, T. F. Liu, R. P. Chen, Y. B. Huang and R. Cao, *Angew. Chem. Int. Edit.*, 2020, **59**, 23641-23648.

43. F. P. García de Arquer, C.-T. Dinh, A. Ozden, J. Wicks, C. McCallum, A. R. Kirmani, D.-H. Nam, C. Gabardo, A. Seifitokaldani and X. Wang, *Science*, 2020, **367**, 661-666.

44. G. Wang, J. Chen, Y. Ding, P. Cai, L. Yi, Y. Li, C. Tu, Y. Hou, Z. Wen and L. Dai, *Chem. Soc. Rev.*, 2021, **50**, 4993-5061.

45. J.-C. Jiang, J.-C. Chen, M.-d. Zhao, Q. Yu, Y.-G. Wang and J. Li, *Nano Res.*, 2022, **15**, 7116-7123.

46. S. Chen, B. Wang, J. Zhu, L. Wang, H. Ou, Z. Zhang, X. Liang, L. Zheng, L. Zhou and Y.-Q. Su, *Nano Lett.*, 2021, **21**, 7325-7331.

47. Y. Cai, J. Fu, Y. Zhou, Y.-C. Chang, Q. Min, J.-J. Zhu, Y. Lin and W. Zhu, *Nat. Commun.*, 2021, **12**, 1-9.

48. H.-L. Zhu, J.-R. Huang, X.-W. Zhang, C. Wang, N.-Y. Huang, P.-Q. Liao and X.-M. Chen, *ACS Catal.*, 2021, **11**, 11786-11792.

49. Z. Han, D. Han, Z. Chen, J. Gao, G. Jiang, X. Wang, S. Lyu, Y. Guo, C. Geng and L. Yin, *Nat. Commun.*, 2022, **13**, 1-10.

50. X. Zheng, B. Li, Q. Wang, D. Wang and Y. Li, *Nano Res.*, 2022, **15**, 7806-7839.

51. R. Ding, M. Ma, Y. Chen, X. Wang, J. Li, G. Wang and J. Liu, *Nano Res.*, 2023, **16**, 264-280.

52. G. Huang, Q. Niu, Y. He, J. Tian, M. Gao, C. Li, N. An, J. Bi and J. Zhang, *Nano Res.*, 2022, **15**, 8001-8009.

53. G. Wang, Y. Wu, Z. Li, Z. Lou, Q. Chen, Y. Li, D. Wang and J. Mao, *Angew. Chem. Int. Edit.*, 2023, **62**, e202218460.

54. T. Gan and D. Wang, *Nano Res.*, 2023, 1-21.

55. Z. Wang, Q. Yuan, J. Shan, Z. Jiang, P. Xu, Y. Hu, J. Zhou, L. Wu, Z. Niu and J. Sun, *J. Phys. Chem. L*, 2020, **11**, 7261-7266.

56. H. Hashiba, H. K. Sato, S. Yotsuhashi, K. Fujii, M. Sugiyama and Y. Nakano, *Sustain Energ Fuels*, 2017, **1**, 1734-1739.

57. H. Pan and C. J. Barile, *Energ. Environ. Sci.*, 2020, **13**, 3567-3578.

58. Y. Hori, A. Murata and R. Takahashi, *Journal of the Chemical Society, Faraday Transactions 1: Physical Chemistry in Condensed Phases*, 1989, **85**, 2309-2326.

59. J. J. Kim, D. P. Summers and K. W. Frese Jr, *J. Electroanal. Chem. Interfacial Electrochem.*, 1988, **245**, 223-244.

60. Z. Sun, T. Ma, H. Tao, Q. Fan and B. Han, *Chem*, 2017, **3**, 560-587.

61. J. Shen and D. Wang, *Nano Res. Energy*, 2023, , **2**, e9120096 .

62. W. Luo, X. Nie, M. J. Janik and A. Asthagiri, *ACS Catal.*, 2016, **6**, 219-229.

63. C. Xie, Z. Niu, D. Kim, M. Li and P. Yang, *Chem. Rev.*, 2019, **120**, 1184-1249.

64. Y. Hori, H. Wakebe, T. Tsukamoto and O. Koga, *Surf. Sci.*, 1995, **335**, 258-263.

65. Y. Hori, I. Takahashi, O. Koga and N. Hoshi, *J. Mol. Catal. A: Chem.*, 2003, **199**, 39-47.

66. D. Gao, R. M. Arán-Ais, H. S. Jeon and B. Roldan Cuenya, *Nat. Catal.*, 2019, **2**, 198-210.

67. R. Reske, H. Mistry, F. Behafarid, B. Roldan Cuenya and P. Strasser, *J. Am. Chem. Soc.*, 2014, **136**, 6978-6986.

68. Z. Zhuang, L. Xia, J. Huang, P. Zhu, Y. Li, C. Ye, M. Xia, R. Yu, Z. Lang and J. Zhu, *Angew. Chem. Int. Edit.*, 2022, **62**, e202212335.

69. Z. Liu, Y. Du, R. Yu, M. Zheng, R. Hu, J. Wu, Y. Xia, Z. Zhuang and D. Wang, *Angew. Chem. Int. Edit.*, 2022, **62**, e202212653.

70. R. Li and D. Wang, *Nano Res.*, 2022, **15**, 6888-6923.

71. J. Yang, W. H. Li, K. Xu, S. Tan, D. Wang and Y. Li, *Angew. Chem. Int. Edit.*, 2022, **134**, e202200366.

72. E. Zhang, L. Tao, J. An, J. Zhang, L. Meng, X. Zheng, Y. Wang, N. Li, S. Du and J. Zhang, *Angew. Chem. Int. Edit.*, 2022, **134**, e202117347.

73. S. Ning, H. Ou, Y. Li, C. Lv, S. Wang, D. Wang and J. Ye, *Angew. Chem. Int. Edit.*, e202302253, **62**, e202302253.

74. L. Wang, H. Liu, J. Zhuang and D. Wang, *Small Sci.*, 2022, **2**, 2200036.

75. Q. Wang, X. Zheng, J. Wu, Y. Wang, D. Wang and Y. Li, *Small Struct.*, 2022, **3**, 2200059.

76. A. M. Argo, J. F. Odzak and B. C. Gates, *J. Am. Chem. Soc.*, 2003, **125**, 7107-7115.

77. C. J. H. Jacobsen, S. Dahl, P. L. Hansen, E. Törnqvist, L. Jensen, H. Topsøe, D. V. Prip, P. B. Møenshaug and I. Chorkendorff, *J. Mol. Catal. A: Chem.*, 2000, **163**, 19-26.

78. W. H. Li, B. C. Ye, J. Yang, Y. Wang, C. J. Yang, Y. M. Pan, H. T. Tang, D. Wang and Y. Li, *Angew. Chem. Int. Edit.*, 2022, **61**, e202209749.

79. K. Manthiram, B. J. Beberwyck and A. P. Alivisatos, *J. Am. Chem. Soc.*, 2014, **136**, 13319-13325.

80. Q. Hu, Z. Han, X. Wang, G. Li, Z. Wang, X. Huang, H. Yang, X. Ren, Q. Zhang and J. Liu, *Angew. Chem. Int. Edit.*, 2020, **59**, 19054-19059.

81. W. H. Li, J. Yang and D. Wang, *Angew. Chem. Int. Edit.*, 2022, **61**, e202213318.

82. T. Cui, Y. P. Wang, T. Ye, J. Wu, Z. Chen, J. Li, Y. Lei, D. Wang and Y. Li, *Angew. Chem. Int. Edit.*, 2022, **61**, e202115219.

83. X. Zheng, J. Yang, Z. Xu, Q. Wang, J. Wu, E. Zhang, S. Dou, W. Sun, D. Wang and Y. Li, *Angew. Chem. Int. Edit.*, 2022, **61**, e202205946.

84. B. Wang, C. Cheng, M. Jin, J. He, H. Zhang, W. Ren, J. Li, D. Wang and Y. Li, *Angew. Chem. Int. Edit.*, 2022, **134**, e202207268.

85. M. Qu, Z. Chen, Z. Sun, D. Zhou, W. Xu, H. Tang, H. Gu, T. Liang, P. Hu and G. Li, *Nano Res.*, 2023, **16**, 2170-2176.

86. F. Yang, H. Yu, Y. Su, J. Chen, S. Chen, Z. Zeng, S. Deng and J. Wang, *Nano Res.*, 2023, **16**, 146-154.

87. A. Han, W. Sun, X. Wan, D. Cai, X. Wang, F. Li, J. Shui and D. Wang, *Angew. Chem. Int. Edit.*, **62**, e202303185.

88. X. Zheng, J. Yang, P. Li, Z. Jiang, P. Zhu, Q. Wang, J. Wu, E. Zhang, W. Sun and S. Dou, *Angew. Chem. Int. Edit.*, 2023, **62**, e202217449.

89. A. Bagger, W. Ju, A. S. Varela, P. Strasser and J. Rossmeisl, *ACS Catal.*, 2019, **9**, 7894-7899.

90. Y. Xu, F. Li, A. Xu, J. P. Edwards, S.-F. Hung, C. M. Gabardo, C. P. O'Brien, S. Liu, X. Wang and Y. Li, *Nat. Commun.*, 2021, **12**, 2932.

91. Y. Hori, R. Takahashi, Y. Yoshinami and A. Murata, *J. Phys. Chem. B*, 1997, **101**, 7075-7081.

92. N. Gupta, M. Gattrell and B. MacDougall, *J. Appl. Electrochem.*, 2006, **36**, 161-172.

93. C.-T. Dinh, T. Burdyny, M. G. Kibria, A. Seifitokaldani, C. M. Gabardo, F. P. García de Arquer, A. Kiani, J. P. Edwards, P. De Luna and O. S. Bushuyev, *Science*, 2018, **360**, 783-787.

94. H. S. Jeon, J. Timoshenko, C. Rettenmaier, A. Herzog, A. Yoon, S. W. Chee, S. Oener, U. Hejral, F. T. Haase and B. Roldan Cuenya, *J. Am. Chem. Soc.*, 2021, **143**, 7578-7587.

95. J. Zhu, L. Xia, R. Yu, R. Lu, J. Li, R. He, Y. Wu, W. Zhang, X. Hong and W. Chen, *J. Am. Chem. Soc.*, 2022, **144**, 15529-15538.

96. Y. Gao, B. Liu and D. Wang, *Adv. Mater.*, **35**, 2023, 2209654.

97. A. Murata and Y. Hori, *B. Chem. Soc. Jpn.*, 1991, **64**, 123-127.

98. G. Z. Kyriacou and A. K. Anagnostopoulos, *J. Appl. Electrochem.*, 1993, **23**, 483-486.

99. A. S. Varela, W. Ju, T. Reier and P. Strasser, *ACS Catal.*, 2016, **6**, 2136-2144.

100. J. Resasco, Y. Lum, E. Clark, J. Z. Zeledon and A. T. Bell, *Chem. Electro. Chem.*, 2018, **5**, 1064-1072.

101. X. Wang, P. Ou, J. Wicks, Y. Xie, Y. Wang, J. Li, J. Tam, D. Ren, J. Y. Howe and Z. Wang, *Nat. Commun.*, 2021, **12**, 3387.

102. H. Zhang, X. Chang, J. G. Chen, W. A. Goddard Iii, B. Xu, M.-J. Cheng and Q. Lu, *Nat. Commun.*, 2019, **10**, 3340.

103. C. F. C. Lim, D. A. Harrington and A. T. Marshall, *Electrochim. Acta*, 2017, **238**, 56-63.

104. H. Zhang, X. Chang, J. G. Chen, W. A. Goddard, B. Xu, M.-J. Cheng and Q. Lu, *Nat. Commun.*, 2019, **10**, 1-9.

105. X. Wang, P. Ou, J. Wicks, Y. Xie, Y. Wang, J. Li, J. Tam, D. Ren, J. Y. Howe and Z. Wang, *Nat. Commun.*, 2021, **12**, 1-7.

106. C. G. Morales-Guio, E. R. Cave, S. A. Nitopi, J. T. Feaster, L. Wang, K. P. Kuhl, A. Jackson, N. C. Johnson, D. N. Abram and T. Hatsukade, *Nat. Catal.*, 2018, **1**, 764-771.

107. S. Wei, X. Jiang, C. He, S. Wang, Q. Hu, X. Chai, X. Ren, H. Yang and C. He, *J. Mater. Chem. A*, 2022, **10**, 6187-6192.

108. Q. Zhao, Y. Wang, M. Li, S. Zhu, T. Li, J. Yang, T. Lin, E. P. Delmo, Y. Wang and J. Jang, *SmartMat*, 2022, **3**, 183-193.

109. L. Lin, T. Liu, J. Xiao, H. Li, P. Wei, D. Gao, B. Nan, R. Si, G. Wang and X. Bao, *Angew. Chem. Int. Edit.*, 2020, **59**, 22408-22413.

110. H. Zou, G. Zhao, H. Dai, H. Dong, W. Luo, L. Wang, Z. Lu, Y. Luo, G. Zhang and L. Duan, *Angew. Chem. Int. Edit.*, **62**, 2022.

111. Y. Wang, Z. Chen, P. Han, Y. Du, Z. Gu, X. Xu and G. Zheng, *ACS Catal.*, 2018, **8**, 7113-7119.

112. L. Xue, C. Zhang, J. Wu, Q.-Y. Fan, Y. Liu, Y. Wu, J. Li, H. Zhang, F. Liu and S. Zeng, *Appl. Catal. B-Environ.*, 2022, **304**, 120951.

113. S. Chen, Z. Zhang, W. Jiang, S. Zhang, J. Zhu, L. Wang, H. Ou, S. Zaman, L. Tan and P. Zhu, *J. Am. Chem. Soc.*, 2022, **144**, 12807-12815.

114. B. J. Fisher and R. Eisenberg, *J. Am. Chem. Soc.*, 1980, **102**, 7361-7363.

115. N. Furuya and K. Matsui, *J. Electroanal. Chem. Interfacial Electrochem.*, 1989, **271**, 181-191.

116. J. Shen, R. Kortlever, R. Kas, Y. Y. Birdja, O. Diaz-Morales, Y. Kwon, I. Ledezma-Yanez, K. J. P. Schouten, G. Mul and M. T. M. Koper, *Nat. Commun.*, 2015, **6**, 8177.

117. H. Xiao, W. A. Goddard Iii, T. Cheng and Y. Liu, *P. Natl. Acad. Sci.*, 2017, **114**, 6685-6688.

118. L. L. Zhuo, P. Chen, K. Zheng, X. W. Zhang, J. X. Wu, D. Y. Lin, S. Y. Liu, Z. S. Wang, J. Y. Liu and D. D. Zhou, *Angew. Chem. Int. Edit.*, 2022, **134**, e202204967.

119. A. Guan, Z. Chen, Y. Quan, C. Peng, Z. Wang, T.-K. Sham, C. Yang, Y. Ji, L. Qian and X. Xu, *ACS Energy Lett.*, 2020, **5**, 1044-1053.

120. W. Ju, A. Bagger, X. Wang, Y. Tsai, F. Luo, T. Möller, H. Wang, J. Rossmeisl, A. S. Varela and P. Strasser, *ACS Energy Lett.*, 2019, **4**, 1663-1671.

121. J. Wang, M. Zheng, X. Zhao and W. Fan, *ACS Catal.*, 2022, **12**, 5441-5454.

122. S. Ren, D. Joulié, D. Salvatore, K. Torbensen, M. Wang, M. Robert and C. P. Berlinguette, *Science*, 2019, **365**, 367-369.

123. Y. Cai, J. Fu, Y. Zhou, Y.-C. Chang, Q. Min, J.-J. Zhu, Y. Lin and W. Zhu, *Nat. Commun.*, 2021, **12**, 586.

124. C. Huang, Y. Li, N. Wang, Y. Xue, Z. Zuo, H. Liu and Y. Li, *Chem. Rev.*, 2018, **118**, 7744-7803.

125. X. Gao, H. Liu, D. Wang and J. Zhang, *Chem. Soc. Rev.*, 2019, **48**, 908-936.

126. R. Lang, X. Du, Y. Huang, X. Jiang, Q. Zhang, Y. Guo, K. Liu, B. Qiao, A. Wang and T. Zhang, *Chem. Rev.*, 2020, **120**, 11986-12043.

127. K. L. Zhou, Z. Wang, C. B. Han, X. Ke, C. Wang, Y. Jin, Q. Zhang, J. Liu, H. Wang and H. Yan, *Nat. Commun.*, 2021, **12**, 1-10.

128. D. Gao, Y. Zhang, Z. Zhou, F. Cai, X. Zhao, W. Huang, Y. Li, J. Zhu, P. Liu and F. Yang, *J. Am. Chem. Soc.*, 2017, **139**, 5652-5655.

129. L. Lv, R. Lu, J. Zhu, R. Yu, W. Zhang, E. Cui, X. Chen, Y. Dai, L. Cui and J. Li, *Angew. Chem. Int. Edit.*, 2023, **62**, e202303117.

130. Z. Zhang, S. Chen, J. Zhu, C. Ye, Y. Mao, B. Wang, G. Zhou, L. Mai, Z. Wang and X. Liu, *Nano Lett.*, 2023, **23**, 2312-2320.

131. Y. Jiang, Q. Chen, D. Wang, X. Li, Y. Xu, Z. Xu and G. Guo, *Nano Res.*, 2023, 16, 6661-6669.

132. J. Xu, S. Yang, L. Ji, J. Mao, W. Zhang, X. Zheng, H. Fu, M. Yuan, C. Yang and H. Chen, *Nano Res.*, 2023, **16**, 53-61.

133. Z. Weng, Y. Wu, M. Wang, J. Jiang, K. Yang, S. Huo, X.-F. Wang, Q. Ma, G. W. Brudvig and V. S. Batista, *Nat. Commun.*, 2018, **9**, 415.

134. A. D. Handoko, F. Wei, Jenndy, B. S. Yeo and Z. W. Seh, *Nat. Catal.*, 2018, **1**, 922-934.

135. S.-F. Hung, A. Xu, X. Wang, F. Li, S.-H. Hsu, Y. Li, J. Wicks, E. G. Cervantes, A. S. Rasouli and Y. C. Li, *Nat. Commun.*, 2022, **13**, 819.

136. D. Karapinar, N. T. Huan, N. Ranjbar Sahraie, J. Li, D. Wakerley, N. Touati, S. Zanna, D. Taverna, L. H. Galvão Tizei and A. Zitolo, *Angew. Chem. Int. Edit.*, 2019, **58**, 15098-15103.

137. Z. Zhang, J. Zhu, S. Chen, W. Sun and D. Wang, *Angew. Chem. Int. Edit.*, 2023, **135**, e202215136.

138. X. Li, X. Yang, J. Zhang, Y. Huang and B. Liu, *ACS Catal.*, 2019, **9**, 2521-2531.

139. D. Zang, X. J. Gao, L. Li, Y. Wei and H. Wang, *Nano Res.*, 2022, **15**, 8872-8879.

140. C. E. Creissen and M. Fontecave, *Nat. Commun.*, 2022, **13**, 2280.

141. J. Zhang, X. Song, L. Kang, J. Zhu, L. Liu, Q. Zhang, D. J. L. Brett, P. R. Shearing, L. Mai and I. P. Parkin, *Chem Catal.*, 2022, **2**, 3254-3270.

142. W. Wang, X. Wang, Z. Ma, Y. Wang, Z. Yang, J. Zhu, L. Lv, H. Ning, N. Tsubaki and M. Wu, *ACS Catal.*, 2022, **13**, 796-802.

143. W. Zhang, C. Huang, J. Zhu, Q. Zhou, R. Yu, Y. Wang, P. An, J. Zhang, M. Qiu and L. Zhou, *Angew. Chem. Int. Edit.*, 2022, **61**, e202112116.

144. X. Li, S. Wang, L. Li, Y. Sun and Y. Xie, *J. Am. Chem. Soc.*, 2020, **142**, 9567-9581.

145. S. Ren, E. W. Lees, C. Hunt, A. Jewlal, Y. Kim, Z. Zhang, B. A. W. Mowbray, A. G. Fink, L. Melo and E. R. Grant, *J. Am. Chem. Soc.*, 2023, **145**, 4414-4420.

146. N. Corbin, J. Zeng, K. Williams and K. Manthiram, *Nano Res.*, 2019, **12**, 2093-2125.

TOC

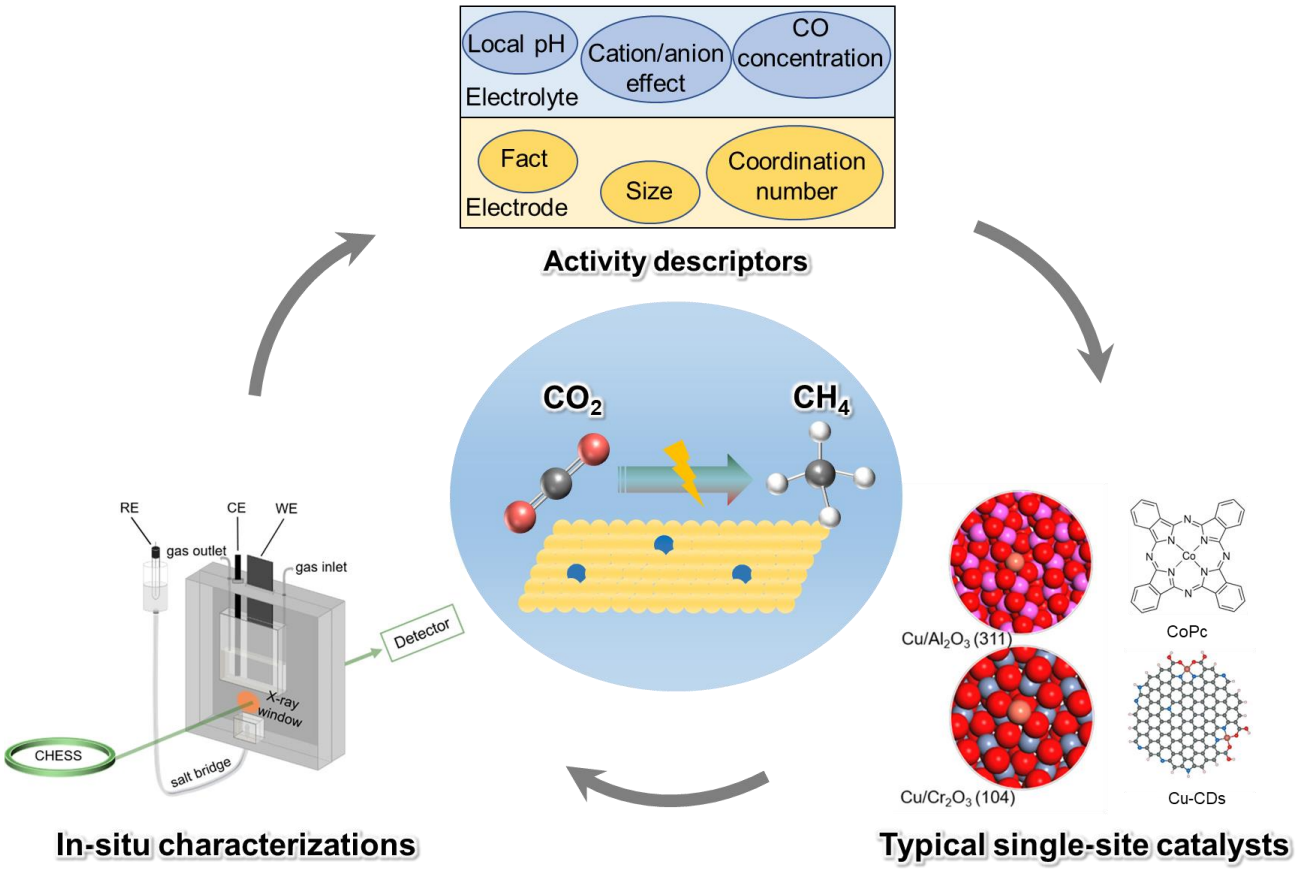

In this review, we systematically summarizes the recent advances and challenges of electrocatalytic CO_2 methanation on single-sites catalysts. The key parameters which greatly influence the selectivity of CO_2 methanation, the recent advances of SSCs on different substrates for electrocatalytic CO_2 methanation, and some in-situ characterizations used for tracking the structure change of SSCs during CO_2RR are discussed in detail.